Mon. Not. R. Astron. Soc. **000**, 1-30 (2009) Printed 4 April 2009 (MN LATEX style file v2.2)

On the variation of black hole accretion disc radii as a function of state and accretion rate

C. Cabanac[1⋆], R. P. Fender[1], R. J. H. Dunn[1,2]† and E. G. Körding[1,3]
[1] *School of Physics and Astronomy, University of Southampton, Southampton SO17 1BJ, UK*
[2] *Excellence Cluster Universe, Technische Universität München, 85748 Garching, Germany*
[3] *AIM - Unité Mixte de Recherche CEA - CNRS - Université Paris VII - UMR 7158, CEA-Saclay, Service d'Astrophysique, F-91191 Gif-sur-Yvette Cedex, France*

arXiv:0904.0701v1 [astro-ph.HE] 4 Apr 2009

Accepted 2009 April 02. Received 2009 April 02; in original form 2008 November 27

ABSTRACT

In response to major changes in the mass accretion rate within the inner accretion flow, Black hole binary transients undergo dramatic evolution in their X-ray timing and spectral behaviour during outbursts. In recent years a paradigm has arisen in which 'soft' X-ray states are associated with an inner disc radius at, or very close to, the innermost stable circular orbit (ISCO) around the black hole, while in 'hard' X-ray states the inner edge of the disc is further from the black hole. Models of advective flows suggest that as the X-ray luminosity drops in hard states, the inner disc progressively recedes, from a few gravitational radii (R_g) at the ISCO, to hundreds of R_g. Recent observations which show broad iron line detections and estimates of the disc component strength suggest that a non-recessed disc could still be present in bright hard states. In this study we present a comprehensive analysis of the spectral components associated with the inner disc, utilising bright states data from X-ray missions with sensitive low-energy responses(e.g. *Swift, SAX*), including reanalyses of previously published results. A key component of the study is to fully estimate systematic uncertainties associated with such spectral fits. In particular we investigate in detail the effect on the measured disc flux and radius of having a hydrogen column density that is fixed or free to vary. We conclude that at X-ray luminosities above ~ 0.01 of the Eddington limit, systematic uncertainties only allow us to constrain the disc to be $\lesssim 10R_g$ from spectral fits. There is, however, clear evidence that at X-ray luminosities between 10^{-2}–10^{-3} of the Eddington rate, the disc does begin to recede. We include measurements of disc radii in two quiescent black hole binaries at bolometric luminosities of $< 10^{-7}$ Eddington, and present the inferred evolution of disc luminosity, temperature, inner radius and accretion rate/efficiency across the entire range of bolometric luminosities 10^{-8}–1 Eddington. We compare our results with theoretical models, and note that the implied rate of disc recession with luminosity is consistent with recent empirical results on the X-ray timing behaviour of black holes of all masses.

Key words: Accretion, accretion discs – X-rays: binaries.

1 INTRODUCTION

The large changes in the X-ray spectra, radio fluxes and timing properties observed among the states of the BHBs are commonly explained with models involving a variation of the accretion efficiency and rate. This variation of the efficiency can be caused by the inward or outward motion of the inner radius of the optically thick accretion disc $R_{\rm in}$ (see e.g., Esin 1997). Recently, a number of papers have been published contesting this radius evolution.

Since the first X-ray spectral studies of Cyg X-1 (Tananbaum et al. 1972) and A0620-00 (Coe et al. 1976), BHBs in outburst seem to transit between what are now commonly identified as "canonical states". Those variations were subsequently associated with changes in radio emission and the timing characteristics of the X-ray emission. A dichotomy could clearly be identified, resulting in the the characterisation of two states. In one state the spectrum is dominated by a thermal optically thick component,

⋆ E-mail: c.cabanac@astro.soton.ac.uk (CC)
† Alexander von Humboldt Fellow

is hereafter called the soft or "Thermal Dominant" (TD) (McClintock & Remillard 2003b) state. The other state, the so-called *hard* state, has a powerlaw shape X-ray spectrum extending up to a few hundreds of keV (see e.g., McConnell et al. 2002 for the differences observed in Cyg X-1 spectra).

Those objects exhibit ejections that are observed in radio and infrared and that occur in particular states (Fender & Belloni 2004). Although steady and compact jets are typical of the hard state, the ejection process appears to be quenched whenever it enters in the soft state (Fender et al. 1999). Fender, Belloni & Gallo (2004) give simple physical interpretations of the observed correlations, resulting from which promising elaborate models based on accretion-ejection solutions in magnetised discs have been built-up (see e.g., Ferreira et al. 2006 and references therein for an auto-similar analysis of the problem, but also Machida, Nakamura & Matsumoto 2006).

For the vast majority of models invoked, the transition between the two main canonical states has been interpreted as follows. In the soft state, usually occurring at a high luminosity (i.e. $0.01 < L_{\rm bol}/L_{\rm Edd} < 1$), the geometrically thin and optically thick accretion disc is believed to reach the Innermost Stable Circular Orbit[1] (ISCO). However, in order to reproduce the decreasing disc efficiency observed in the hard states, the inner part of the disc is truncated and replaced by a radiatively inefficient and optically thin flow. The accreted mass is either advected towards the central black-hole (ADAF and equivalent: Esin 1997; Narayan et al. 1997) or part of it is ejected in outflows, for example, an ADIOS (Blandford & Begelman 2004) or a Jet Emitting Disc (JED, Ferreira et al. 2006) are examples of structures that could explain the observed behaviour.

XMM-Newton observations of GX 339-4 (Miller et al. 2006a, hereafter M06) cast doubt on this accepted interpretation by showing that a broad iron line together with a dim, hot thermal component was present in its spectra during the hard state. This effect seems to be observed in a few other sources such as Cygnus X-1, and SWIFT J1753.5-0127 (M06, Miller et al. 2006b). However, all of these conclusions are based on single observation without studying the overall evolution during an outburst of the source.

A robust way of evaluating the disc inner geometry value is to choose the same approach as Gierliński & Done, (2004). They followed the disc parameter value during the outburst rise and decline. In the simplistic hypothesis of an optically thick disc extending down to the last stable orbit of the black-hole, one would expect that the relationship between the disc luminosity $L_{\rm disc}$ and the inner temperature $T_{\rm in}$ should be monotonic; $L_{\rm disc} = K_{\rm disc} T_{\rm in}^4$ with $K_{\rm disc}$ constant, whatever the accretion rate. When the value of $R_{\rm in}$ is much lower than $R_{\rm out}$, then $K_{\rm disc} \sim 4\pi R_{\rm in}^2 \sigma_B$.

Recently, Rykoff et al. (2007) (hereafter R07) performed a similar analysis on the black hole candidate XTE J1817-330. They reported that no noticeable changes could be observed in the inner disc radii values, even when reaching the hard state. On the contrary, taking into account the effect of irradiation, Gierliński, Done & Page (2008) argue that a significant increase in $R_{\rm in}$ could be measured. One of the goals of this paper is to disentangle this apparent discrepancy.

[1] The ISCO isequal to 6 R_g for a Schwarzschild BH, or 2 R_g for a fully spinning Kerr BH.

Table 1. Orbital parameters used for the whole study.

Source	Mass ($M_\odot$)	Distance (kpc)	i (^{o})
J1118+480	$(8.53 \pm 0.6)^a$	$(1.72 \pm 0.10)^a$	$(68 \pm 2)^a$
GX 339-4	$(7^{12}_{5.8})^b$	$(8^{9.4}_{6.7})^c$	$(30^{60}_{20})^d$
J1655-40	$(6.3 \pm 0.5)^e$	$(3.2^{3.4}_{1.7})^f$	$(70^{71}_{64})^g$
J1817-330	$(6^{10}_{3.5})^h$	$(6.3^{10}_{2.6})^h$	$(60)^h$
J1753.5-0127	$(6^{12}_{5})^i$	$(2.9^{10}_{2.9})^i$	$(60)^i$
A0620-00	$(11 \pm 1.9)^j$	$(1.16 \pm 0.11)^j$	$(40.75 \pm 3)^j$

[a] Gelino et al. (2006).
[b] Hynes et al. (2003) for the mass function.
[c] Zdziarski et al. (2004).
[d] Compatible with Cowley et al. (2002).
[e] Greene, Bailyn & Orosz (2001)
[f] Hjellming & Rupen (1995) for the value but we used Foellmi et al. (2006) as a lower limit.
[g] van der Hooft et al. (1998).
[h] S07 for the mass and distance, however see the text for the lower limit in distance. Arbitrary inclination.
[i] Mostly arbitrary but average values expected for BHB. See Miller et al. (2006b) for the low limit in distance.
[j] Gelino et al. (2001).

Source sample and data selection criteria.

Considering the large amount of data available in archives, it was necessary to select the data used in this study. The data were selected according to the following criteria: first, we focused on X-ray transients, as they allow to follow a source on broader luminosity range. As we focus on the lowest luminosity states and the study of the thermal component, data coming from instruments with good sensitivity at low energy (typically under 1 keV) were preferred, ruling out e.g. RXTE archives. For these reasons, the Swift/XRT data seemed to be ideal as it tends to follow the outburst of a source by taking a number of different snapshots over time. A major part of this analysis will therefore be based on data from this instrument. Lastly, confirmed black hole binaries were favoured, as we wanted to make comparisons among different sources using e.g. Eddington luminosities and hence masses and distances. However, as the outbursts of XTE J1817-330 and Swift J1753.5-0127 were well sampled, we also added them into our sample even though they have not been confirmed as black hole binaries. According to these criteria, our sample reduces to 6 sources: **XTE J1118+480, GX 339-4, GRO J1655-40, XTE J1817-330, Swift J1753.5-0127 and A 0620-00** (see Tab. 1 for the adopted masses, angles and distances).

2 DATA REDUCTION AND REANALYSIS

The purpose of our paper is to extend previous studies of the disc parameters to lower disc luminosities, as well as to systematically and uniformly test spectral models. There

are two approaches that can be chosen to overcome the difficulties of determining the parameter values of the disc. The first is to try to fit the spectra with the best models available. This means using sophisticated comptonisation codes or tables to fit the hard component, and the possible reprocessing of hard X-rays on the optically thick disc. The main advantage is to usually obtain better fits to the spectra. This comes at a price, of having a larger number of free parameters. The other main drawback when adopting this approach is that comparison among sources or different observations is difficult as the models chosen are not necessarily the same.

The other method consists of using the simplest model, involving the least number of parameters. This allows the same simple model to be fitted to the spectra resulting from every source and observation. The price which is paid is a lower goodness of fit, but it allows comparisons among sources to be made.

We choose to adopt this latter approach in our study. The spectra were fitted with a powerlaw at high energy and any possible soft component by a multicolour disc. We also added the photoelectric absorption of the neutral hydrogen in the line of sight. Therefore the number of free parameters in the model does not exceed five: the absorption $N_{\rm H}$, the multicolour disc temperature $T_{\rm in}$ and normalisation $K_{\rm disc}$, and the powerlaw photon index Γ and normalisation $K_{\rm PL}$. However, in order to study the effect of changing the high energy emission model on the conclusions drawn, we also used a thermal comptonisation model (`compTT` in XSPEC) for some of the observations. As the value of the high-energy cutoff was usually unavailable, we therefore fixed the value of the temperature of the thermal electron to 50 keV unless stated otherwise. The number of free parameters are therefore still reduced to two for this component: the optical depth and the normalisation.

2.1 Precision of the cross-analysis

In this paper we pay particular attention to comparisons among several sources (Section 5), which involves different orbital parameters and distances, disc radius or luminosities have all been rescaled in terms of the gravitational radius $\rm R_g = GM/c^2 = 1.48 M/M_\odot$ km and Eddington luminosity $L_{\rm Edd} = 1.48 \times 10^{38} (M/\rm M_\odot)$ erg s^{-1} (e.g., Gierliński & Done, 2004). Depending on the disc inclination and for projection reasons we use:

$$\frac{L_{\rm disc}}{L_{\rm Edd}} = \frac{F_{\rm disc}}{L_{\rm Edd}} \times \frac{2\pi d^2}{\cos(i)} \quad (1)$$

$$= 4 \times 10^5 \times \frac{F_{\rm disc}\, {d_{\rm kpc}}^2}{M_{\rm M_\odot} \cos(i)}, \quad (2)$$

where $d_{\rm kpc}$ is the distance expressed in kpc, $F_{\rm disc}$ the disc luminosity in erg cm^{-2} s^{-1}, $M_{\rm M_\odot}$ the black hole mass expressed in solar masses, and i the inclination angle ($i = 0$ is a "face-on" disc).

Assuming that the hard component emits isotropically, we have approximately:

$$\frac{L_{\rm hard}}{L_{\rm Edd}} = 8 \times 10^5 \times \frac{F_{\rm hard}\, d_{\rm kpc}^2}{M_{\rm M_\odot}}, \quad (3)$$

For the evaluation of the disc parameters, and for the reasons explained above, we use the simple multicolour disc model (`diskbb` in XSPEC, see e.g., Mitsuda et al. 1984). Several drawbacks have already been pointed out concerning this model as it neglects processes such as increased scattering at high temperatures, or the differential emission that can occur between different altitudes in the disc (the central part of the disc may be warmer). Such drawbacks mainly affect the effective temperature compared to the observed one. However, the temperature shift is only 4% for a 0.5 keV disc and this effect decreases with decreasing temperature (Gierliński & Done, 2004). The fact that we aimed to probe the lowest luminous states also motivated our choice to use a simple `diskbb` to model the thermal component.

As $R_{\rm in}$ is obtained via the normalisation ($K_{\rm disc} = (R_{\rm in,\ km}/d_{10\ \rm kpc})^2 \cos(i)$ in XSPEC) of the multicolour disc model, it gives:

$$\frac{R_{\rm in}}{\rm R_g} = 0.677 \left(\frac{d}{10\ \rm kpc}\right) \left(\frac{M}{\rm M_\odot}\right)^{-1} \left(\frac{K_{\rm disc}}{\cos(i)}\right)^{0.5}. \quad (4)$$

Unless mentioned explicitly in the text, all errors in this paper will also be expressed in terms of 90% (1.64 σ) confidence range (including the plots).

2.2 XTE J1118+480: multiwavelength campaigns

2.2.1 In outburst

For the study of the BHB XTE J1118+480, we mainly used the parameters given in the literature. The number of observations where a thermal component is required in the spectra are quite scarce, as there is just the one coming from the 2000 outburst and one other, during quiescence in 2002. Among the articles dealing with this outburst where a thermal component is observed, two were based on a multiwavelength study including UV data (McClintock et al. 2001 and Chaty et al. (2003), hereafter (MC01) and (Ch03)) whereas the other focused on results given by Beppo-SAX data (Frontera et al. 2003).

We note a particular issue regarding the parameter of the disc obtained by MC01. There seems to be an inconsistency between the low value of the radius given in the text when using a simple multicolour disc to fit the HST and EUVE data, and the spectrum given in their Fig. 3. They obtain an internal radius of 34 $\rm R_S$ ($1\rm R_S = 2R_g$), and an internal temperature of 24 eV. Such a model, (assuming as (MC01) do, $M = 6\rm M_\odot$, $d = 1.8$ kpc and $i = 80^{\rm o}$) should peak at a value of $\nu F_\nu \sim 10^{-11.8}$ erg cm^{-2} s^{-1}. From their Spectral Energy Distribution (SED) it is clear that this is about two orders of magnitude lower than the peak value shown in the third panel (i.e. $\nu F_\nu \sim 10^{-8.6}$ erg cm^{-2} s^{-1}). In order to obtain a similar value with their orbital parameters and temperature, we have to set $K_{\rm disc} \sim 7 \times 10^8$. This then gives us $R_{\rm in} \sim 300 R_{\rm S}$ when we take into account the orbital values displayed in our Tab. 1.

This is moreover consistent with the value of $R_{\rm in} \sim 352 R_{\rm S}$ obtained by (Ch03) based on the same data set (HST, EUVE, CXC, RXTE, UKIRT and Ryle telescope), where SAX and the VLA data were added, and modelled by the same simple multicolour disc + powerlaw(s). The small residual differences could come from the value of the absorption adopted by each authors ($N_{\rm H} = 1.1 \times 10^{20}$ cm^{-2}

for (Ch03) and $N_{\rm H} = 1.3 \times 10^{20}$ cm^{-2} for (MC01)), and the secondary contribution in optical as well.

However, when using SAX data in their multi-wavelength analysis, (Ch03) did not take into account the lowest energy bins (0.13-26 keV) as the flux value conflicts with the EUVE ones. They argued that this discrepancy could come from calibration issues in SAX responses at low energy. However, as the amount of available observations for XTE J1118+480 outburst is quite low, we have tried to include these data in our study. This is also supported by the fact that in studies based on the full SAX broad band spectrum (Frontera et al. 2001, 2003), a thermal component was also detected though peaking at a higher energy (∼50 keV) than those given in (MC01) and (Ch03). However in Frontera et al. (2003), the low energy part of the spectrum was fitted with a single black-body spectrum and thus we tried to probe the effect of reanalysing the data with a multicolour disc.

Therefore, we used and reanalysed the processed LECS (low-energy concentrator spectrometer, 0.1-4 keV, Parmar et al. 1997), MECS (medium-energy concentrator spectrometer, 1.8-10.5 keV Boella et al. 1997) and PDS (Phoswich Detector System, 10-200 keV, Frontera et al. 1997) spectra available on the archive for both "ToO1" (ObsId 21173001) and "ToO3" (ObsId 211730012) observations mentioned in Frontera et al. (2003). The usual response files were used, we allowed a free normalisation among the three instruments and one per cent systematics were also added. As pointed out by Frontera et al. (2003), the addition of a thermal component to the absorbed cutoff power-law model is necessary. When we add a `diskbb` (the absorption being free to vary), the reduced χ^2 drops from $\chi^2/\nu = 286.05/191 = 1.50$ to 213.64/189=1.130 (F-test probability = 1.05×10^{-12}) in ToO1 (from $\chi^2/\nu = 2.98$ to 1.25 in ToO3) . We noted also that taking a single black body for the thermal component gives similar goodness of fit as in that case $\chi^2/\nu = 212.60/189 = 1.126$ in ToO1 for example. As stated before, we thus kept the results coming from a multicolour disc. The results of the fits to the disc parameters are given in Tab. C of the appendix.

We note that the results we obtain for the thermal component are quite different between the SAX data and the EUVE data, as was pointed out in (Ch03). The value of the disc flux is about 10 times lower in SAX data, the temperature is about three times higher than in the EUVE. However the major difference comes from the normalisation of the multicolour disc as it is 10^3 lower. This means the disc is closer to the central black hole by a factor 30. As there is no obvious reasons to favour one or the other set of data, we decided to keep both of them, and infer that the real state of the disc should be between both. In the following figures, results coming from both data sets are displayed explicitly.

2.2.2 In quiescence

For the analysis in quiescence, we mainly based our analysis on the results coming from McClintock et al. (2003a) (MC03a). Compared to those authors, we did some slight corrections to estimate disc radii and luminosities for XTE J1118+480, given the accuracy of the orbital parameters obtained since then by Gelino et al. (2006). For example, with the value of the internal radius that (MC03a) obtain (around 3100 $R_{\rm g}$ but for $M = 7M_{\odot}$, $d = 1.8$ kpc and $i = 80^o$), we derived the corresponding `diskbb` normalisation ($K_{\rm disc}$).

We then added the temperature estimate to evaluate the net disc flux contribution ($F_{\rm disc} \propto K_{\rm disc} T^4$). Subsequently we corrected the luminosities and the internal radius from the newest orbital parameter in order to obtain $R_{\rm in} \sim 1640$ $R_{\rm g}$, $L_{\rm hard} \sim 1.3 \times 10^{-8}$ $L_{\rm Edd}$ and $L_{\rm bol} \sim 7.7 \times 10^{-8}$ $L_{\rm Edd}$. Note that, except for the disc temperature, no statistical errors coming from the fits were available for the luminosities nor the radius inferred and hence those latter are not displayed in the figures of the study.

2.3 A0620-00: HST/STIS and Chandra

In order to estimate the disc properties of A0620-00, we used the values published by (MC03a), McClintock et al. (2000) and McClintock et al. (1995) as following. We have already pointed out that the lack of optical-UV observation of the source (compared to XTE J1118+480) is still a major problem as we are not sure that a multicolour disc is the best model to fit the data. We noted that MC03a, McClintock et al. (2000) interpreted those data in the framework of an ADAF, whereas in our study we try to explain the possible UV extra component in the context of a multicolour disc.

Another limitation concerning this source comes from the fact that the X-ray and optical observations were not simultaneous. Therefore the conclusions resulting from this object must be taken with caution.

However, concerning the disc properties, and due to the simplicity of the model, we only had to find a rough estimate of the inner temperature and the normalisation of the `diskbb`. For the temperature, we note that the HST/STIS disc spectrum obtained by McClintock et al. (2000) in 1998 was very similar to the one obtained six years before (comparing Fig. 2 of McClintock et al. 2000 and Fig. 5 of McClintock et al. 1995). Hence, we took the 9000 K (7.7×10^{-4} keV) black body spectrum (McClintock et al. 1995) as a reference for the temperature value. A `diskbb` spectrum with such a temperature value peaks nearby 3500 Å, as it was also observed in the 1998 spectrum.

This temperature value fixed, we then obtained the normalisation of the `diskbb` model via the flux value at 4×10^{-3} keV, which is around $\nu F_{\nu} \sim 10^{-12.4}$ erg cm^{-2} s^{-1}. It thus gave us $K_{\rm disc} \sim 2.8 \times 10^{11}$. Hence, the corresponding radius would be (following mass, distance and angle value of Tab. 1): $R_{\rm in} = 4.5 \times 10^3$ $R_{\rm g}$. The bolometric flux of the disc component is $F_{\rm disc} = 2.3 \times 10^{-12}$ erg cm^{-2} s^{-1}.

For the hard X-ray component, we took the powerlaw model given by (MC03a) where the photon index value is given as $\Gamma = 2.26$. We inferred the normalisation value of the powerlaw considering that the flux value at 1 keV is $\nu F_{\nu} \sim 10^{-14}$ erg cm^{-2} s^{-1} (see Fig. 11 of MC03a). The corresponding absorbed ($N_{\rm H} = 1.94 \times 10^{20}$ cm^{-2}, see MC03a) bolometric (0.02-200 keV) flux is then $F_{\rm pl} = 4.3 \times 10^{-14}$ erg cm^{-2} s^{-1}.

2.4 GX 339-4: ASCA/GIS data

For the three ASCA/GIS observation of GX 339-4 (see Wilms et al. 1999 for a previous study), we also explored

the influence of the $N_{\rm H}$ value on the disc parameters. Again, for consistency we fitted the data by a simple absorbed `diskbb+powerlaw` (Wilms et al. 1999 used a broken powerlaw, a choice that might influence the radius estimate). We chose to probe this effect using three different ways. Firstly by fixing the absorption value to the one adopted by Wilms et al. (1999), i.e. $N_{\rm H,\ 1} = 0.62 \times 10^{22}$ cm^{-2} (see also Zdziarski et al. 1998), then by fixing it to the weighted mean average value we obtained in the following study with *Swift* data (see Section 3), i.e. $N_{\rm H,\ 2} = 0.43 \times 10^{22}$cm^{-2}, and finally by leaving it free to vary. Results of those fits are given in Tab. 2.

As noticed with the *Swift* data, the value of the disc normalisation tends to decrease whenever the absorption does. For example in the third observation the corresponding internal radius would reach a value of ~ 17 R$_{\rm g}$ when the value of the absorption is fixed to $N_{\rm H} = 0.62 \times 10^{22}$ cm^{-2}, and drops to ~ 1 R$_{\rm g}$ when it is left free to vary. The disc is not even necessary in order to fit the spectra properly when using a floating $N_{\rm H}$ in observation one and two. However, it is unclear whether this is due to a real trend or a systematical effect linked to ASCA/GIS data analysis.

A good way of disentangling this problem would consist in applying the same processes we did for *Swift* data (see Section 3). However, as the the number of observations is quite low in this case (3 observations compared to more than 20), we would not be able to draw definite conclusions. As a result of this, we chose to keep the results coming from the case when $N_{\rm H}$ is fixed to 0.43×10^{22} cm^{-2} (average value obtained with *Swift*) for the following study.

2.5 XTE J1817-330, SWIFT J1753.5-0127, GRO J1655-40 and GX 339-4: *Swift* data

For XTE J1817-330, we processed the data in the same way as in R07 (especially concerning the region sizes for the pile-up correction) except that we used the XRT pipeline software version 0.11.5 (2007-08-23 release date) and more recent response files coming from the CALDB 20071101 version (v009) as well. Of particular importance are the better corrections to the residuals under 0.6 keV in WT mode compared to earlier response files. It allows us to perform spectral fitting within the 0.3-10 keV energy range though adding 3% of systematics (Campana et al. 2007).

For GX 339-4, GRO J1655-40 and SWIFT J1753.5-0127 especially in WT mode, the pile-up correction was done using the second method as described in Mineo et al. (2007) and recapped here. For a given observation, different annuli (PC mode) or boxes (WT mode) of decreasing sizes were extracted in the images and spectra were generated and fitted with the most convenient model (either a powerlaw or a powerlaw+disc). Then when the fit parameter reach the asymptotic values obtained with the smallest annuli/boxes[2], it determines the maximal size of the admitted region.

For spectra obtained in LrPD mode (GRO J1655-40, see also Brocksopp et al. 2005), spectra have been fitted in the 0.5-10 keV range. However, we noticed that the value of 5 per cent given by Cusumano et al. (2005) tends to lead to particularly low χ^2 values. We obtain an average value of the reduced χ^2 of about ~ 0.6 on 13 observations. We therefore investigated the effect of changing the value of the systematics on the calculation of the errors on the fit parameters. Changing the systematics from 2.5 per cent to 5 per cent, the relative errors on e.g. the absorption value in obs. 00030009005 jumps from only 1.1 per cent to 1.7 per cent. The disc normalisation changes from 3.1 per cent to 4.6 per cent. Therefore, if the systematics seem overestimated in LrPD mode, the actual value has little effect on our study. We therefore kept the 5 per cent given in Cusumano et al. (2005).

For certain observations where the disk is dominating, the addition of a powerlaw gives an unrealistic photon index value (sometimes negative). For those latter cases, we did not take into account the 7.5-10 keV energy range (as Brocksopp et al. 2005 do). The addition of a powerlaw is thus sometimes not required. Spectra were also binned in order to get at least 20 counts/channel.

For any given observation of the source, there can exist gaps due to Good-Time-Interval (GTI). In the early version of the XRT data processing software somewhere the spectra for each GTI had to be extracted separately, this effect is now taken into account. However, we decided to keep this process when fitting spectra, i.e. for one observation we can get several spectra and thus different fit parameter values. As we wanted to probe any effect on the disc even when quite dim, this way of processing allows to check if any change in the disc parameters would be due to a temporary instrumental bias.

2.6 Fits and flux estimate methods

Unless explicitly mentioned, all spectra in this study were fitted using XSPEC v12.3.1ao (Arnaud 1996). We also used the `fluxerror` tcl script based on Monte-Carlo method that was provided by K. Arnaud. It allows the estimation of flux errors on each component of the model separately. However, we slightly modified the script in order to be able to compute the errors within an extended energy range instead of the default one. In order to estimate the bolometric luminosity, absorbed flux computation has thus been performed between 0.05 and 200 keV for the hard component. This choice was motivated by the fact that:

(i) the cut-off observed in hard states generally occurs around a few hundred keV or the flux contribution over 200 keV is low for typical soft state (with $\Gamma \sim 2.5$, $F_{\rm pl,\ 200.-20000\ keV}/F_{\rm pl,\ 2.-200\ keV} = 0.1$).

(ii) there should also exist a "cut-off" of the powerlaw at low energy (taken into account when fitting by e.g., thermal comptonisation models) that can be roughly mimicked by the absorption.

A summary of the fit results used in this study for the disc geometry analysis (i.e. Sections 4, 5 and 6) are displayed in Tabs. A, B and C.

[2] In our case, if the photon index differences are less than 5 per cent of the asymptotic value.

Table 2. Results of the fits by an absorbed `diskbb+powerlaw` of GX 339-4 ASCA/GIS spectra when changing the absorption value.

	$N_{\rm H}$ value	$K_{\rm disc}$	$kT_{\rm in}$	$F_{\rm disc}$	$F_{\rm pl}$	χ^2/ν
Obs #1	0.62	$8.2^{16}_{4.6} \times 10^3$	0.19 ± 0.02	$2.3^{2.7}_{1.5} \times 10^{-10}$	$9.0 \pm 0.3 \times 10^{-10}$	1054.03/954
	0.43	$1.1^{6.1}_{0.29} \times 10^3$	$0.21^{0.27}_{0.17}$	$5.1^{6.3}_{0} \times 10^{-11}$	$1.003^{1.006}_{0.997} \times 10^{-9}$	1030.70/954
	0.32 ± 0.02 (free)			powerlaw only sufficient		1025.03/954
Obs #2	0.62	$2.4^{4.0}_{1.6} \times 10^4$	0.18 ± 0.01	$5.5^{6.0}_{4.7} \times 10^{-10}$	$1.55 \pm 0.05 \times 10^{-9}$	1279.46/1174
	0.43	$7.8^{40}_{1.9} \times 10^3$	0.17 ± 0.04	$1.4^{1.4}_{0.} \times 10^{-10}$	$1.75^{1.81}_{1.70} \times 10^{-9}$	1201.70/1174
	0.29 ± 0.01 (free)			powerlaw only sufficient		1184.69/1175
Obs #3	0.62	$3.37^{3.89}_{3.04} \times 10^4$	$0.211^{0.214}_{0.206}$	$1.38^{1.49}_{1.37} \times 10^{-9}$	$4.00^{4.04}_{3.93} \times 10^{-9}$	2970.47/1469
	0.43	$2.68^{3.16}_{2.30} \times 10^3$	$0.279^{0.288}_{0.270}$	$3.42^{3.63}_{3.41} \times 10^{-10}$	$4.63^{4.71}_{4.55} \times 10^{-9}$	2506.09/1469
	0.27 ± 0.01 (free)	135^{190}_{100}	$0.46^{0.50}_{0.26}$	$1.31^{1.46}_{1.15} \times 10^{-10}$	$5.37^{5.53}_{5.24} \times 10^{-9}$	2366.47/1468

3 THE HYDROGEN COLUMN DENSITY: TO FIX OR NOT TO FIX?

The value of the hydrogen column density adopted is always a central problem when trying to constrain the properties of the disc. For many previous studies (R07, Gierliński & Done, 2004) this value was fixed, either by referring to the most common adopted values (e.g., Gierliński & Done, 2004), or by taking the one inferred by the fit at the highest fluxes.

Studying the geometrical properties of the optically thick disc via X-ray analysis is always a challenge as one has to determine the value of two parameters that appear to be quite correlated - the column density and the normalisation of the emitting disc (that is proportional to its projected area). Moreover, this degeneracy will be strengthened by intrinsic and/or technical effects; the lower the maximum temperature of the disc, the higher the column density or the lower the spectral sensitivity of the instrument observing, the higher the degeneracy.

For example, even for sources like GRO J1655-40 or GRS 1915+105 that show high disc temperatures during their outburst, several authors fix the hydrogen column density value when using RXTE observations (Gierliński & Done, 2004 for example). This is justified as the low efficiency of the PCA under 2 keV would not constrain easily the value of the absorption. However, when using observatories as efficient at low energy as Chandra, XMM or *Swift*, there seems to be fewer "a priori" underlying reasons to fix the $N_{\rm H}$ for every spectral analysis.

In this section we will study the effect of letting the value of $N_{\rm H}$ varying versus keeping it fixed, especially during the transition from soft to hard state. We apply this to the *Swift*-XRT data of GX 339-4, XTE J1817-330, GRO J1655-40 and SWIFT J1753.5-0127. Initially we evaluated the value of $N_{\rm H}$ at the highest luminosities. In that case, its value varies between 4.6 $\times 10^{21}$ to 2 $\times 10^{21}$ cm^{-2} from observation number one to 13 in GX 339-4 data, and between 2 $\times 10^{21}$ to less than 1 $\times 10^{21}$ cm^{-2} for XTE J1817-330 for example. Then, **when a multicolour disc is required** according to our standards (see hereafter in section 4), we can compute the weighted mean value $N_{\rm H,\ wmean}$. It gives $N_{\rm H,\ wmean} = 0.43 \pm 0.02 \times 10^{22}$ cm^{-2} for GX 339-4, $0.12 \pm 0.02 \times 10^{22}$ cm^{-2} for XTE J1817-330 (in agreement with the value obtained by R07), 0.246 ± 0.011 cm^{-2} for SWIFT J1753.5-0127 and 0.73 ± 0.014 cm^{-2} for GRO J1655-40.

If we now plot the dependency between the value of $N_{\rm H}$ and the photon index as shown in the first column of Fig. 1, one can see that there seem to be a slight correlation between the value of $N_{\rm H}$ obtained from one observation to another. That effects can also be seen when looking at the distribution of $N_{\rm H}$ values presented in the left column of Fig. 2.

However, as we combine three different models (`wabs` × (`diskbb` + `powerlaw`) or `wabs` × (`diskbb` + `compTT`)) with a total of five free parameters, one cannot *a priori* exclude a systematic degeneracy among those. Indeed, one can argue that the trend between the photon index and the value of $N_{\rm H}$ obtained could be purely due to the model used, as a higher photon index would require a high absorption to obtain one and the same flux at low energies.

Therefore, in order to probe if the trend was real or due to the fitting process, we proposed to follow the following scheme summarised on Fig. 3. Having processed the *real* data as described above (i.e. with a floating $N_{\rm H}$), in parallel and for each observation we fitted the same spectrum in the same way (i.e. adding a disc, or not, when it was not appropriate), **except that the $N_{\rm H}$ is now fixed to the best weighted mean value obtained above**. With those new fit parameter values, we then faked a spectrum with the XSPEC command `fakeit`, taking the same response files and time elapsed, thus obtaining the so-called *fixed then faked (ff)* spectrum. In a third step, we fitted this *ff* spectrum with a floating $N_{\rm H}$, hence obtaining *fff* (**f**ixed, **f**aked, **f**ree) parameters. The comparisons in the value of $N_{\rm H}$ obtained in the *fff* and in the simple case of a floating $N_{\rm H}$ would allow one to determine whether the observed variation is more consistent with statistic/systematic deviation or with a real trend.

Results are displayed from Fig. 2 to 5 and Tabs. 3, 4 and 5. Two complementary approaches have been used: first by comparing both distributions of $N_{\rm H}$ obtained, and then the apparent photon index Γ-$N_{\rm H}$ correlation observed. As stated in the previous section, both cases where the high energy part of the spectrum is fitted with either a powerlaw or a `comptt` Titarchuk et al. (1994) model were examined. Both analysis seems to be useful, as it seems to lead to different conclusions.

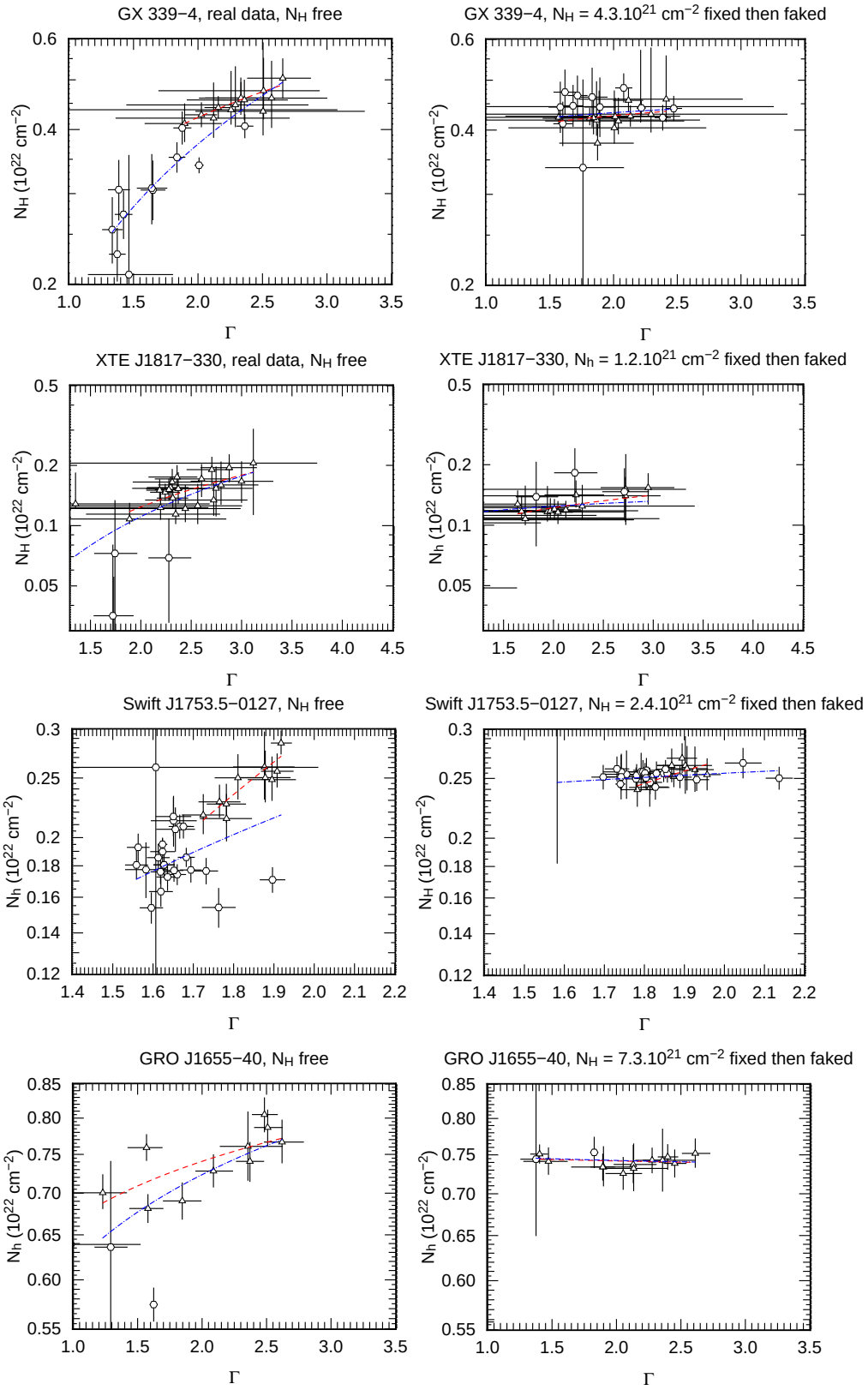

Figure 1. Column density variation during the transition in GX 339-4, XTE J1817-330, SWIFT J1753.5-0127 and GRO J1655-40 when high energy component in real and faked data are fitted with a powerlaw model. The model is either a $wabs*po$ (○) or a $wabs*(diskbb+po)$ (△). Dashed line shows the fit by a powerlaw of the △ and the dotted-dashed line is a fit of all acceptable points (△ and ○ when $\Gamma > 1$). See Tab. 3 for the fit results. Note that for some observations a powerlaw component is not necessary to fit the spectra (e.g for GRO J1655-40). Therefore the number of points in those graphs can be different from the numbers given in the histograms of Fig. 2.

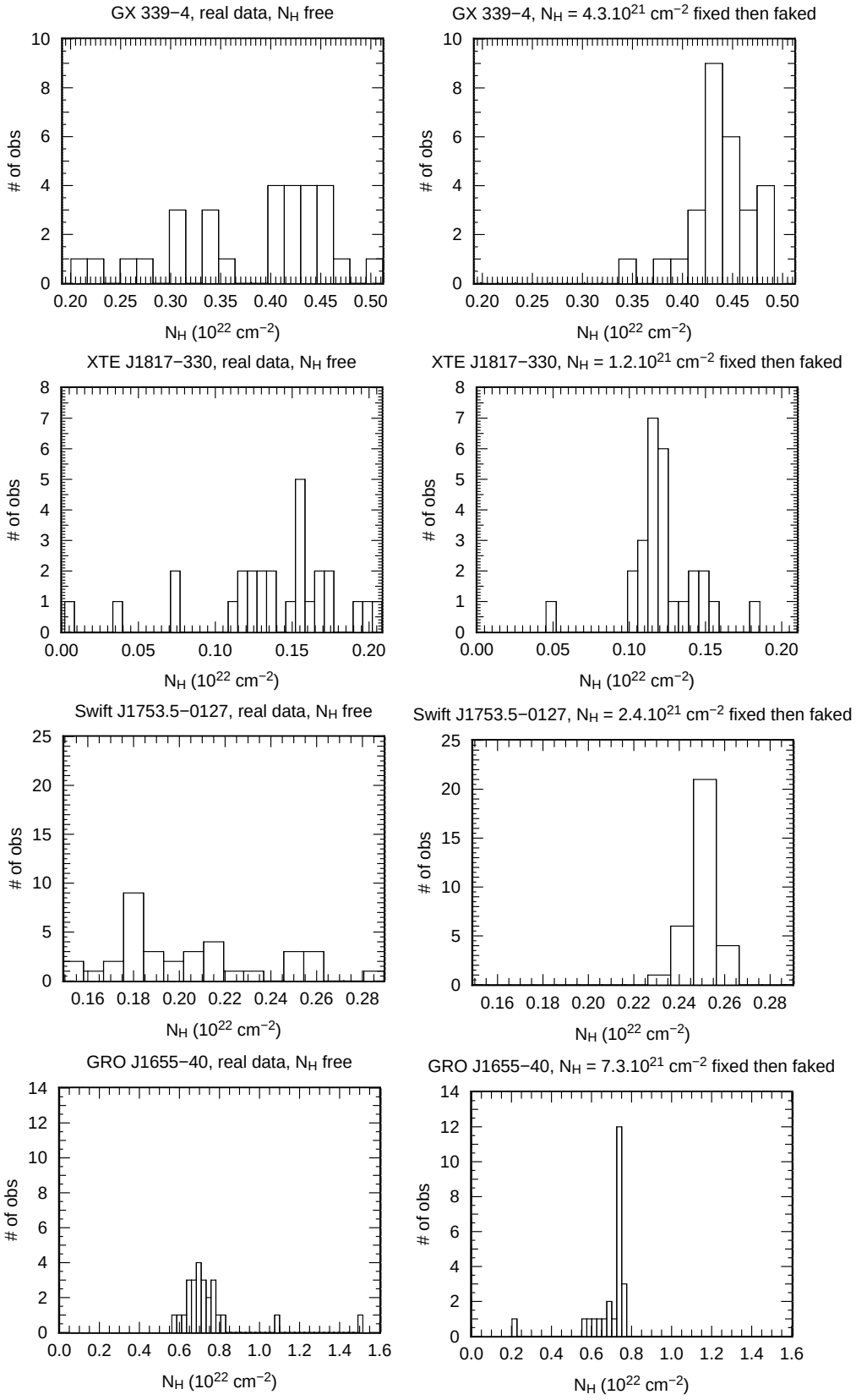

Figure 2. Distribution of $N_{\rm H}$ when the high energy component in real and faked data are fitted with a powerlaw model. Left panels correspond to the real data fitted with a floating $N_{\rm H}$, when the right panels correspond to data obtained by faking the real data when $N_{\rm H}$ is fixed to the weighted mean value obtained in the highest states.

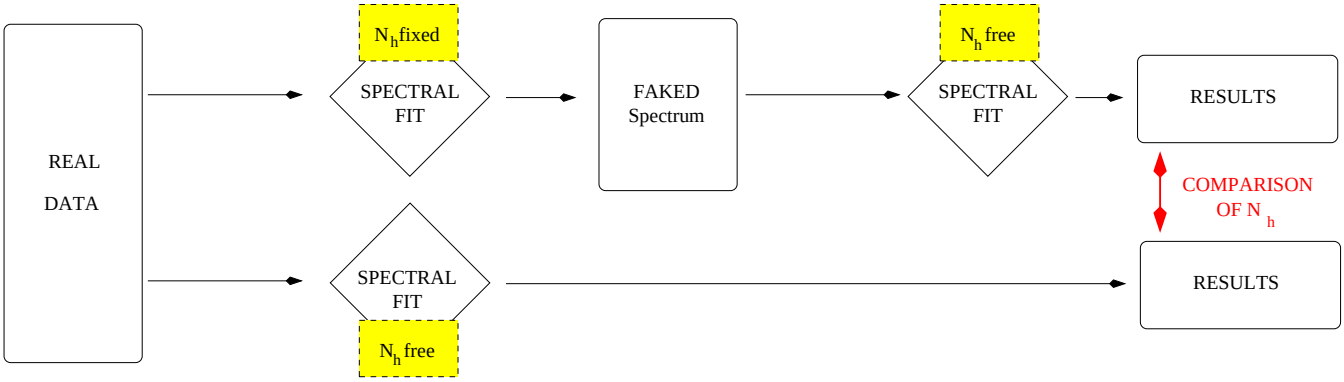

Figure 3. Schematic process we adopted to probe if the variation in the column density value observed was a systematic effect of data analysis or real. This comparison is called the *fff method* in the text.

3.1 High energy component fitted by a powerlaw.

When a powerlaw is used first, one can see in the histograms of Fig. 2 the relative differences between the distribution of $N_{\rm H}$ obtained in the real and the faked spectra. As a result, if we except the case of GRO J1655-40, the real distributions seems to be flatter than the *fff* ones. We then performed a Kolmogorov-Smirnov (KS) test to compare the latter distributions. The results, shown on Tab. 5, give a low probability that the real and the *fff* spectra could come from the same distribution. However, except for SWIFT J1753.5-0127, the KS test probabilities obtained are still too high to draw any definite conclusions.

Had the fitted $N_{\rm H}$ been an artifact of the degeneracy with the fit parameter, we would have expected the distribution to be similar. To confirm the non degeneracy, we fitted the $N_{\rm H}$ versus Γ by a powerlaw in both real and *fff* cases as shown on Fig. 1. Note that the choice of a powerlaw is completely arbitrary. However, it seems straightforward to probe whether there is a systematic trend by examining and comparing the exponent value obtained: a nil value of this latter would for example mean that $N_{\rm H}$ is independent of Γ. We performed this fit using either the whole dataset (dotted-dashed curve in Fig. 1), or only the observations where a disc is required (dashed curve). For the χ^2 evaluation when fitting, each point in the $N_{\rm H}$ vs Γ diagram is weighted according to its error on $N_{\rm H}$ only. The powerlaw exponent values obtained are thus displayed in Tab. 3.

If we pay attention to the real spectra when a disc is required, the exponent values range from a weak dependency of 0.15 in GRO J1655-40 to a bigger one of 2.25 in SWIFT J1753.5-0127. The accuracy of these exponent value is higher than 2.5σ for the four sources studied. If we now examine the values obtained with the `fff` spectra, we note that the exponent is still positive, except for GRO J1655-40, suggesting a possible degeneracy. However, the $N_{\rm H}$ vs Γ dependency is lower in the `fff` case, as shown in in Tab. 3. The exponent values obtained in the real case are always higher than those obtained in the *fff* case by a factor 2.5 to 4.7. Examination of the same analysis performed on the whole dataset (right hand side of Tab. 3) gives similar results.

We then conclude that if a powerlaw is used as model to fit the high energy part of the spectrum, the value of $N_{\rm H}$ seems to vary during the evolution of the source, and *Swift*/XRT is able to detect this evolution. As a result, we suggest to keep $N_{\rm H}$ as a free parameter when fitting *Swift*/XRT data with this model[3], and, we suggest to use the `fff` method for further $N_{\rm H}$ variation studies with other observatories.

3.2 High energy component fitted by comptonisation model.

As the underlying processes resulting in the high energy tail are still under debate, we also chose to examine if the previous variation of $N_{\rm H}$ was still evident when using another model. We thus chose XSPEC `comptt` model, often used as a physically motivated alternative compared to a powerlaw. But this model has the characteristic to exhibit a low energy "cut-off" (Rayleigh-Jeans part of the seed photons coming from the black-body emission), which can greatly influence our previous analysis. If the "true" emission process is actually not extended to low energy, and a powerlaw (which by definition exhibits no low energy cutoff) is used, one expects the absorption to play the role of an artificial cutoff. Hence the $N_{\rm H}$ value obtained when using a powerlaw will be higher than when using `comptt`.

Thus we reran the previous analysis with this model and the results are displayed in Fig. 4 and 5 and Tabs. 4 and 5. Firstly, we can visually examine *fff* distributions obtained on right-hand side of Fig. 4. We note that instead of being normally distributed around the adopted weighted mean value of $N_{\rm H}$, the *fff* spectra tend here to exhibit a second peak at low $N_{\rm H}$ for GX 339-4 (the six observations where $N_{\rm H} \sim 2 \times 10^{21}$ cm^{-2}) and SWIFT J1753.5-0127 (11 observations with $N_{\rm H} \sim 5 \times 10^{20}$ cm^{-2}). This means that faking data with a constant $N_{\rm H}$ can, in certain cases when using the `comptt` model and if we refit the same spectrum with a floating absorption, lead to quite significant differences in the $N_{\rm H}$ fitted value. Moreover, examining the KS test results (right hand side of Tab. 5) gives a higher probability that real and *fff* distributions are the same when using `comptt` compared to when using a powerlaw (except for GRO J1655-40). This effect is particularly visible for SWIFT J1753.5-0127 where the KS probability reaches 15 per cent.

In order to probe if any correlation between the state and the value of $N_{\rm H}$ remains, we used the plasma optical

[3] Of course, this will only be valid for high enough $N_{\rm H}$.

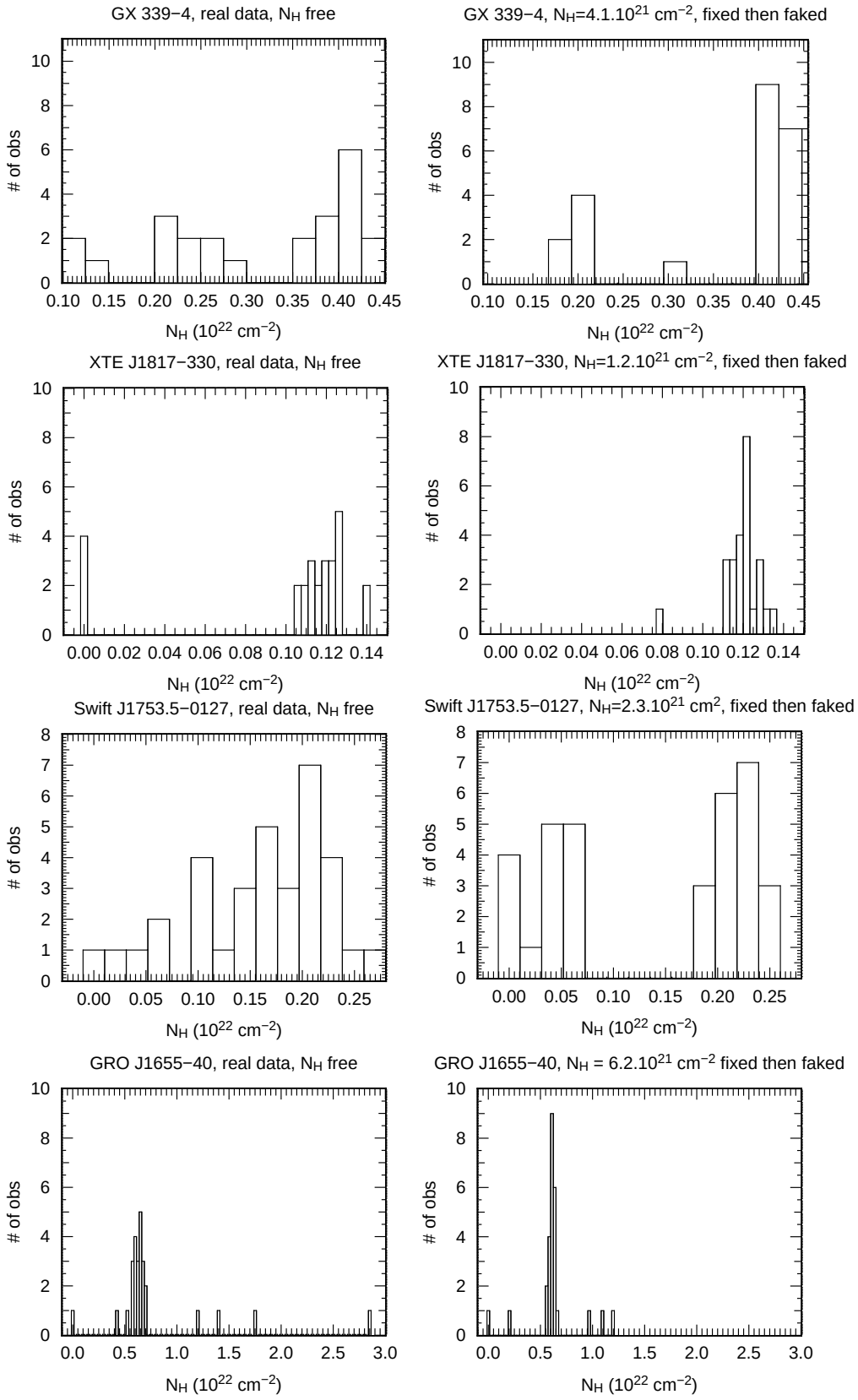

Figure 4. Distribution of $N_{\rm H}$ when high energy component in real and faked data are fitted with the `comptt` model.

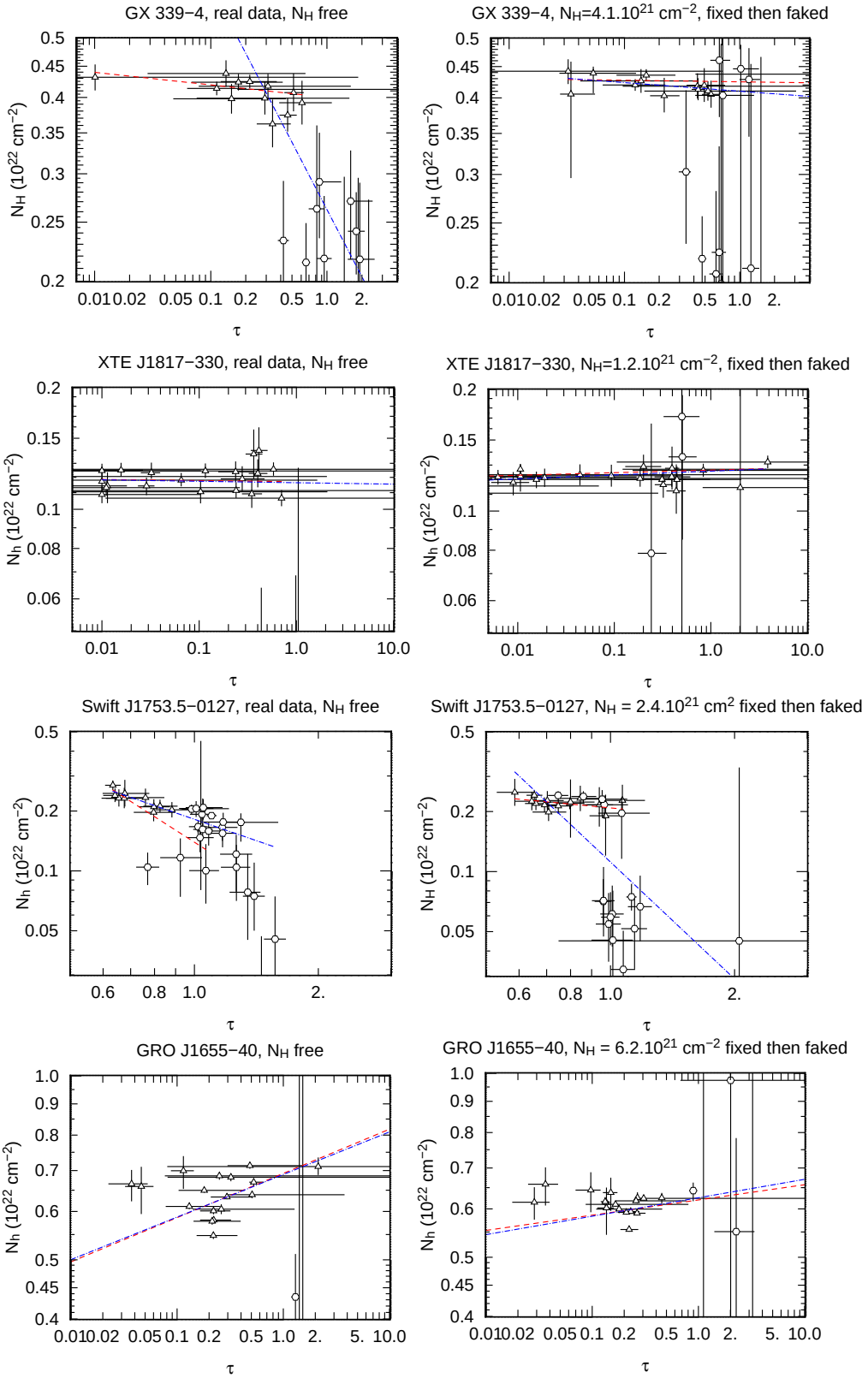

Figure 5. Column density variation during the transition in GX 339-4, XTE J1817-330, SWIFT J1753.5-0127 and GRO J1655-40 when high energy component in real and faked data are fitted with the `comptt` model. See Tab. 4 for the fit results.

Table 3. Result of the fit by a powerlaw plotted on Fig. 1. Dashed line of Fig. 1 correspond to the "only obs. with disc" where dotted-dashed line refers to "all obs.". All uncertainties are 1 σ wide. These results are mainly consistent with a real $N_{\rm H}$ versus Γ correlation, however partly due to systematic deviation coming from spectral analysis.

	Model : $N_{\rm H} = \alpha \times \Gamma^{\beta}$			
Source	β (only obs. with disc)		β (all obs.)	
	real	*fff*	real	*fff*
GX 339-4	0.47 ± 0.05	0.10 ± 0.09	0.98 ± 0.14	0.09 ± 0.06
XTE J1817-330	0.85 ± 0.32	0.35 ± 0.14	1.11 ± 0.39	0.14 ± 0.10
SWIFT J1753.5-0127	2.25 ± 0.38	0.86 ± 0.35	1.16 ± 0.40	0.15 ± 0.09
GRO J1655-40	0.15 ± 0.06	-0.009 ± 0.014	0.23 ± 0.11	-0.01 ± 0.014

Table 4. Results of the fit by a powerlaw plotted on Fig. 5. Every terms have the same signification as Tab. 3. Here, except with XTE J1753.5-0127, there seem to be less correlation between the value of the warm plasma optical depth and the column density.

	Model : $N_{\rm H} = \alpha \times \tau^{\beta}$			
Source	β (only obs. with disc)		β (all obs.)	
	real	*fff*	real	*fff*
GX 339-4	-0.02 ± 0.01	-0.025 ± 0.008	-0.37 ± 0.30	-0.009 ± 0.014
XTE J1817-330	-0.003 ± 0.009	0.008 ± 0.003	-0.004 ± 0.006	0.010 ± 0.003
SWIFT J1753.5-0.127	-0.51 ± 0.16	-0.19 ± 0.14	-0.71 ± 0.14	-1.9 ± 0.3
GRO J1655-40	0.072 ± 0.031	0.025 ± 0.039	0.070 ± 0.030	0.030 ± 0.032

depth value, τ, as an indicator equivalent to the photon index (since Γ depends on the compton parameter y, where $y = kT_e/(m_e c^2) \times max(\tau, \tau^2)$ and T_e is fixed at 50 keV). Fig. 5 illustrates the possible $N_{\rm H}$ vs τ dependency, and fits by powerlaws have been performed as in the previous section. Values of the exponent obtained for observations where a disc is required are consistent with no variation of $N_{\rm H}$ vs τ in GX 339-4, XTE J1817-330 and GRO J1655-40. It is either due to the fact that the value of the exponent is similar between the real and the *fff* spectra (GX 339-4 case), or because its 1σ error for real spectra is as large as the value obtained (XTE J1817-330 case). GRO J1655-40 seems even to show inverse behaviour - the value of the hydrogen column density seems indeed to correlate with the value of the plasma optical depth. On the contrary, SWIFT J1753.5-0127 still seems to exhibit significant decrease of $N_{\rm H}$ when τ increase.

Considering the complete dataset (dot-dashed curve in Fig. 5 and right hand side of Tab. 4) returns similar results, except for SWIFT J1753.5-0127, where the bimodality of *fff* distribution is quite noticeable, forming two separated cluster of points (lower right graph of Fig. 4).

Thus, when using `comptt` to fit the high energy tail of the spectra in *Swift*/XRT data, there is less evidence that the absorption column density is varying. As a result one should view the fitted value of $N_{\rm H}$ with caution. **However, as the statistical errors obtained on τ in this study are quite large, it is difficult to draw definite conclusions about the $N_{\rm H}$ vs τ dependency.** The simultaneous use of an instrument which gives more accurate spectra at higher energy together with our prescribed `fff` method could help to probe any $N_{\rm H}$ vs τ variation. **As a general conclusion, we suggest to leave the absorption free to vary when fitting *Swift*/XRT spectra**.

Table 5. Results given by a KS test probing the probability that the underlying distributions of $N_{\rm H}$ obtained in Fig. 2 are one and the same for the real and the faked spectra.

	`powerlaw`		`comptt`	
KS test:	value	prob.	value	prob.
GX 339-4	0.34	0.048	0.375	0.051
XTE J1817-330	0.41	0.016	0.33	0.09
SWIFT J1753.5-0.127	0.73	7.1×10^{-9}	0.26	0.15
GRO J1655-40	0.28	0.24	0.41	0.017

4 A RECESSING DISC WHEN $L_{\rm BOL} < 10^{-2}\ L_{\rm EDD}$ IN XTE J1817-330?

Although we have just investigated in which cases one has to let the value of $N_{\rm H}$ float during the fitting process, we will examine in this section what is its impact on the disc properties is, especially its geometry. Thus, we will still consider on the one hand, the case when $N_{\rm H}$ is free to vary, and on the other hand, when it is frozen to the value obtained at high luminosity (see Sect. 3 for those values). This work focuses on the *Swift*-XRT observations of XTE J1817-330 which appear to show significant changes in the fitted disc properties during its decline.

Fixing the value of $N_{\rm H}$, or leaving it free during the fitting process has a major impact on the possible detection of a disc component. However, by comparing the effect of adding a `diskbb` model, it seems that in both cases the fit is improved at high luminosity. In the case of an $N_{\rm H}$ value fixed to the one obtained at high luminosities (as opposed to the case where $N_{\rm H}$ is free to vary), taking the example of observation number 13, the χ^2 drops from 13720 to 386.2

(respectively 2281.9 to 380.9) when adding the thermal component.

We now focus particularly on the last four observations of XTE J1817-330 and especially observation number 20. The goodness of fit summary is shown in Tab. 6. Taking into account the degrees of freedom, the situation is less clear, it can show that a simple absorbed powerlaw already gives a relative good fit when the $N_{\rm H}$ is free (reduced $\chi^2 = 1.08$) and adding a `diskbb` in this case suggests an overfitting of the data (the F-test probability is higher than 3 per cent). On the contrary, when the $N_{\rm H}$ is fixed to the value obtained at high luminosity, as the absorption in this latter case is higher, adding an extra component at low energies, like a `diskbb`, will be required (see Tab. 6). This effect is due to the fact that, as we demonstrated in previous sections, when using a powerlaw for the high energy component, the absorption seems to slightly decrease when entering the harder states. Thus an extra component at low energy such as a disc would not be required anymore. On the contrary, if we fix the $N_{\rm H}$ to a high value, then a disc component would be necessary to compensate the flux lost by the absorption.

In the next sections, considering that this effect could affect the possible detection of a disc component, we adopted the following strategy when analysing *Swift* data:

- For easier comparisons and consistency with earlier results given in the bibliography, we fitted the high energy part of the spectra with a powerlaw.
- If ever the spectrum is well fitted by a simple absorbed powerlaw (threshold chosen: $\chi^2/\nu < 1.2$), or if adding a disc component to the latter model gives a high F-test probability (hereafter, $> 10^{-2}$), then no disc component is added.
- On the contrary, when an extra component is necessary, we study the evolution of the parameters and we allowed the absorption to vary (unless it is explicitly mentioned as for XTE J1817-330 case where both varying and fixed $N_{\rm H}$ case were studied).

We can also compare our results with those obtained by R07. For example, in observation number 19 we obtain $\chi^2/\nu = 18.33/23$ with a simple absorbed powerlaw only. The absorption value obtained in this case is quite low ($N_{\rm H} = 7.2 \pm 5 \times 10^{20}$ cm^{-2}), however consistent with earlier Chandra observation (Miller et al. 2006c). Even if we set the $N_{\rm H}$ value to 1.2 $\times 10^{21}$ cm^{-2}, we obtain $\chi^2/\nu = 20.02/24$, which is already sufficient to model the spectrum properly (the addition of a `diskbb` does not improve the fit). It is not clear why R07 added an extra component in that observation. We have similar concerns for obs. 20 and 22. Examining the χ^2 values obtained (see Tab. 6), one can see that adding a disc component is not necessary for the four last observations except, as noted above, in observation number 20. Note also that in obs. 20 the spectrum is only made of 27 channel bins. Performing a F-test between both models (with or without disc) gives a probability of 2×10^{-3}, which is still quite high and still cast doubt on the reliability of adding such thermal component. This disc measurement was however kept for this section's study.

The variation of the hydrogen column density value has also been reported in previous papers involving observations with *Swift* (see e.g. Brocksopp et al. 2005 for the GRO J1655-40 outburst[4]) for objects in their soft state but also in their hard states (Oosterbroek et al. 1996 in V404-Cyg). We also saw in Sect. 2 that ASCA/GIS observations of GX 339-4 can be interpreted in the same framework and lead to different conclusions concerning the absence or the presence of a thermal component whether the value of $N_{\rm H}$ is fixed or not.

We now focus on the remaining observations of XTE J1817-330 at higher luminosity, (observations number two to 17 and even 20 if $N_{\rm H}$ is fixed). When a disc is required, one can track the evolution of the source as its flux is monotonically declining from the first to the last observation (see also Gierliński, Done & Page 2008). As noticed in Gierliński, Done & Page (2008) by contemporaneous observations with RXTE, in the hardness-intensity diagram the source is fading from the high soft state (HS) to the low hard state (LH) by transiting through the lower intermediate state branch (IM) (Homan & Belloni 2005). Note that observations number 15, 16 and 17, of particular interest as we will see, are located in this latter branch.

The whole detailed evolution of the disc properties is displayed in Fig. 6 when using a simple powerlaw as a model to fit the hard component of the spectra, and in Fig. 7 when using `comptt` for the same purpose. As mentioned before, we also examined both the cases where $N_{\rm H}$ is fixed or not: as there are 4 observables ($L_{\rm disc}$, $L_{\rm bol}$, $R_{\rm in}$, $kT_{\rm in}$), there are in theory six 2-dimensional plot combinations. However, for simplicity, we restricted this number to the 4 most important for probing the source evolution and we discarded the $L_{\rm bol}$ vs $L_{\rm disc}$ and the $kT_{\rm in}$ vs $L_{\rm bol}$ plots.

Examination of the first row of graphs in Fig. 6 ($kT_{\rm in}$ vs $L_{\rm disc}$) seems to clearly show an obvious trend: where at high luminosity the temperature seems to decrease monotonically as a unique powerlaw, the last three "double points" (there was two GTIs for each of those three observations) shows a clear drop in temperature. We then tried to fit this $kT_{\rm in}$ vs $L_{\rm disc}$ relationship with two models: first using a simple powerlaw, and second with a broken powerlaw. The fit algorithm uses the standard merit function described in Press et al. (1992), § 6.7. It does take into account both the errors on the Y (inner temperature) and X (luminosity) axis: the principle of this fitting proceedure is described in details in Press et al. (1992), § 15.3, "Straight-Line Data with Errors in Both Coordinates". This algorithm was also used when fitting the $kT_{\rm in}$ vs $R_{\rm in}$ and $L_{\rm bol}$ vs $R_{\rm in}$ relationships.

The results are given in the first set of rows of Tab. 7: first, a simple powerlaw to model those data give a very bad fit, whenever the value of $N_{\rm H}$ is fixed or not ($\chi^2_{\rm spl}/\nu \sim 5.0$ or $\sim 10.$) . Using a broken powerlaw significantly improves the fit as it drops to a value of 1.15 ($N_{\rm H}$ free) or 2.3 ($N_{\rm H}$ fixed). Second, the upper flux powerlaw index (0.27 or 0.26±0.02) is very close to the value expected for a disc emitting with a constant inner radius ($kT_{\rm in} \propto L_{\rm disc}^{0.25}$). By comparison, R07 obtained a powerlaw index equal to 0.233 ± 0.006. It is interesting to note that the second powerlaw index found is quite steep and close to 0.77 ($N_{\rm H}$ free) or 0.6 ($N_{\rm H}$ fixed) at lower flux. The errors on those values, although bigger, are still consistent with a break which would occur at around 0.014 $L_{\rm Edd}$ (with orbital parameters and distance given in

[4] Based on the same data set used in this paper.

Tab. 1). As the temperature seems to suddenly decrease for a rather constant disc luminosity, one expects its normalisation and hence the internal radius to increase in order to compensate for this fall. This is what is examined in the six lower panels of Fig. 6. In observations 16 and 17, the internal radius values double and triple from those measured at higher luminosities.

The second row of Fig. 6 shows the variations of $kT_{\rm in}$ as a function of $R_{\rm in}$. A broken powerlaw has been used again to fit the data. Since for a pure multicolour disc each ring is dissipating the gravitational energy available in radiation as it is optically thick, it can be used as a direct probe of the accretion rate. In that case we have:

$$T_{\rm in} = \left(\frac{3GM\dot{M}_{\rm d}}{8\pi R_{\rm in}^3 \sigma_{\rm B}} \right)^{1/4}, \quad (5)$$

(see e.g Belloni et al. 1997), where $\dot{M}_{\rm d}$ is the mass accretion rate flowing through the disc only. This supposes that 100 per cent of the mass coming from the donor star is accreted entirely through the disc until $R_{\rm in}$. Therefore, renormalising the same formula to Eddington accretion rate and using $L_{\rm Edd} = \eta_{\rm Edd}\dot{M}_{\rm Edd}c^2$, we obtain:

$$\frac{kT_{\rm in}}{1\ {\rm keV}} = 5.31 \left(\frac{M}{{\rm M}_\odot} \right)^{-1/4} \left(\frac{\dot{m}_{\rm d}}{\eta_{\rm Edd}} \right)^{1/4} \left(\frac{R_{\rm in}}{{\rm R_g}} \right)^{-3/4}, \quad (6)$$

where $\dot{m}_{\rm d} = \dot{M}_{\rm d}/\dot{M}_{\rm Edd}$. **Note that $\dot{\mathbf{m}}_{\mathbf{d}} \neq \dot{\mathbf{m}}_{\mathbf{total}}$ in the general case (see for example van der Klis 2001 for evidences of this discrepancy in LMXB)**.

Hence, parallel lines with a slope of (-3/4) can be drawn in a log-log temperature versus radius diagram and the normalisation value only depends on the values of the mass, the radiative efficiency at Eddington luminosity and the accretion rate. This has been done in the second rows of Fig. 6 and 7. Below the apparent break in the relationship, we observe that the disc seems to decrease its accretion efficiency by increasing its radius, keeping its accretion rate constant, especially when $N_{\rm H}$ is kept free. This is further supported by the value of the slope given by the fit even if the errors on it are quite high (-0.70 ± 0.33 consistent with -3/4). By taking $\eta_{\rm Edd} = 0.1$, we conclude then that the accretion rate is close to 0.005 Eddington (± 0.0025 with the large uncertainties on the BH mass). This effect also seems to hold when using a `comptt` (see second row of Fig. 7). Using $L_{disc} = 2\pi R_{\rm in}^2 \sigma_{\rm B} T_{\rm in}^4$, we can easily calculate the value of the accretion rate through the disc[5], i.e.:

$$\dot{m}_d = \frac{2}{3}\eta_{\rm Edd} \left(\frac{L_{\rm disc}}{L_{\rm Edd}} \right) \left(\frac{R_{\rm in}}{{\rm R_g}} \right). \quad (7)$$

Moreover, as variations in the mass ratios of BHBs are far less than those on accretion rates (10^8), one can set a typical mass value (e.g $8{\rm M}_\odot$) and Eddington accretion efficiency (e.g $\eta_{\rm Edd} = 0.1$) in order to estimate the evolution of the accretion rate among different sources. This will be the subject of Section 5.

The beginning of the disc recession can also be noticed in the two last rows of graphs of Fig. 6 and 7 and in Tab. 7 for the results of the fit by a broken powerlaw: the crucial transition observed in the geometry for this source seems then to occur at the same bolometric luminosity level ($\sim 0.015 L_{\rm Edd}$). This is due to the fact that until observation number 15, the disc contributes to more than 90 per cent of the overall luminosity (it drops to 58 per cent in observation 17).

We also compared and included with our results the XMM observation of the source analysed by (Sala et al. 2007, S07). For a better comparison with our data processing manner, we used the fit results that S07 obtained with an absorbed `powerlaw+diskbb`. It appears that the disc normalisation value is still in the range we obtain with *Swift* data in the highest fluxes state (as $K_{\rm disc} \simeq 2000$) although the value of the photon index differs quite a lot when the value of $N_{\rm H}$ is tied to a value of $1.5 \times 10^{21} {\rm cm}^{-2}$. With $\Gamma \simeq 1.6$, the XMM-Newton observation seems to exhibit a non-recessed disc in a low-hard state, similarly to the observations analysed by M06 on GX 339-4. However, if we focus on the value of the fluxes obtained using the fit parameters values given in S07 with $N_{\rm H}$ frozen, it results in an unabsorbed disc flux of $F_{\rm disc} \simeq 1.1 \times 10^{-8}$ erg cm^{-2} s^{-1} and a high absorbed powerlaw flux of $F_{\rm pl} = 2.4 \times 10^{-7}$ erg cm^{-2} s^{-1} in the 0.02-200 keV range. Thus in terms of Eddington luminosity it gives $L_{\rm disc} \sim 0.060\ L_{\rm Edd}$ but $L_{\rm bol} \sim 1.3\ L_{\rm Edd}$ ($M = 6{\rm M}_\odot$, $d = 6.3$ kpc, see Tab. 1). Unless one cannot rule out the possibility that the source lies in our vicinity (i.e $d \sim 1$ kpc, in that case $L_{\rm hard} \sim 0.012\ L_{\rm Edd}$), the overall luminosity is quite high.

We can also note that S07 obtained a much higher photon index ($\Gamma \simeq 2.3$) when letting the value of $N_{\rm H}$ free to vary, but the high energy flux is still completely dominating the spectrum. Such a high bolometric flux is quite puzzling as the closest *Swift*/XRT observations of the source taken 6 days before and two days after (7th and 15th March 2006, corresponding to ObsIDs number 03 and 04) are one order of magnitude less luminous ($L_{\rm bol} \sim 0.13$ and $0.11 L_{\rm Edd}$ respectively). We note however that using `comptt` to model the high energy part of the spectrum gives a more consistent bolometric luminosity value, as in that case $L_{\rm bol} \sim 0.06 L_{\rm Edd}$. The discrepancy could come from the fact that the χ^2 value is far better with this latter model rather than when using a simple powerlaw ($\chi^2/\nu = 1.19$ instead of 1.45). However, in spite of those drawbacks, for the consistency and comparisons among the different sources and observation, we kept these results given by the fit with a powerlaw (with $N_{\rm H}$ free).

In the case that XTE J1817-330 lies at 1kpc, we would also obtain $R_{\rm in} \sim 0.77 \pm 0.05\ {\rm R_g} < {\rm R_S}$ in the highest state of SWIFT data (as estimated from the first five observations). This casts doubt on such a low value for the distance. In order to get at least $R_{\rm in} \sim R_{\rm S}$, one has to set a distance of 2.6 kpc and we thus took this model dependant value as minimal distance to XTE J1817-330 for the following multi-source study. Moreover, if we choose $d = 1kpc$, the beginning of the disc recession observed in SWIFT data would then occur at about $4 \times 10^{-4}\ L_{\rm Edd}$.

[5] Note that the equation number 7 is obtained in the framework of the multicolour disc model. One known limitation is that it gives a quite high accretion efficiency when the radius approach the ISCO, as in that case $\eta(R_{\rm in})_{\texttt{diskbb}} = 3/2({\rm R_g}/R_{\rm in}) = 0.25 \neq 0.06$ when $R_{\rm in} = 6\ {\rm R_g}$ for example.

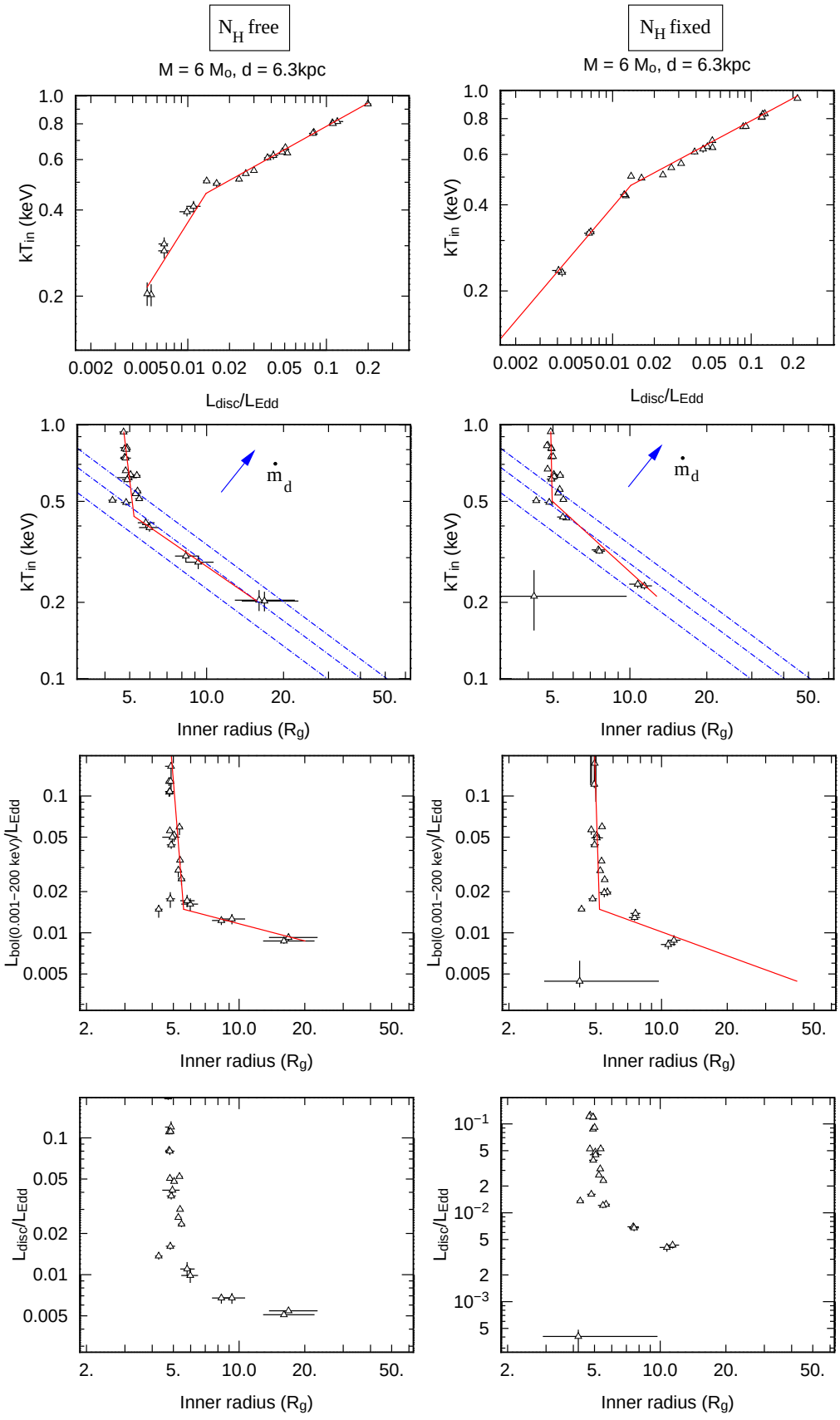

Figure 6. Variation of the disc properties during the decline of XTE J1817-330 when fitting the hard component with a powerlaw. The $kT_{\rm in}$ vs $L_{\rm disc}/L_{\rm Edd}$, $kT_{\rm in}$ vs $R_{\rm in}/{\rm R_g}$ and $L_{\rm bol}/L_{\rm Edd}$ vs $R_{\rm in}/{\rm R_g}$ data sets have been fitted by a broken powerlaw (solid lines, see text and Tab. 7 for the parameters of the fit). The dotted dashed lines plotted in the second row of graphs are showing constant $\dot{m}_{\rm d}$ profile. From upper right to lower left: $\dot{m}_{\rm d} = 0.002,\ 0.005,\ 0.01$ with $\eta_{\rm Edd} = 0.1$.

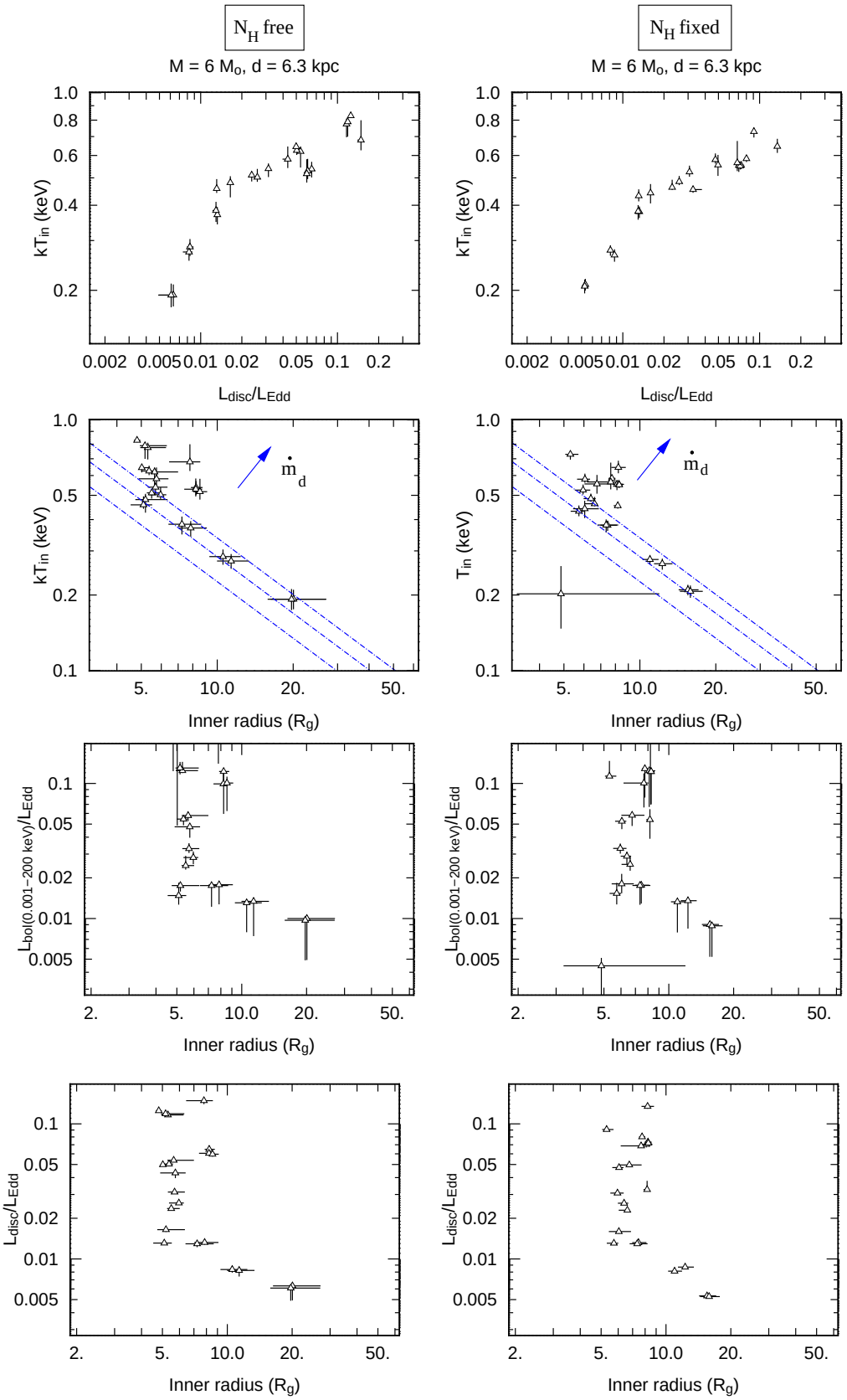

Figure 7. Variation of the disc properties during the decline of XTE J1817-330 when fitting the hard component with the `comptt` model. Here again the beginning of a disc recession seems to be needed. Even if the behaviour at high luminosity is less constant. Same values as in Fig. 6 for $\dot{m}_{\rm d}$ in the second graph row.

Table 6. χ^2 values when fitting the 4 last *Swift* observations of XTE J1817-330 with or without a disc component and using the latest response files. Even when $N_{\rm H}$ is fixed to 0.12×10^{22} cm^{-2}, the reduced χ^2 is quite good enough (i.e. < 1.15) to model the data with a simple powerlaw in observations 19, 21 and 22. Adding a disc component would overfit the data in this case. Note that the values of the f-test probability are just informative as its use is controversial for such small data sets (Protassov et al. 2002).

	χ^2/ν			
Model	Obs. 19	Obs. 20	Obs. 21	Obs. 22
wabs×po	$\frac{18.33}{23} = 0.80$	$\frac{25.89}{24} = 1.08$	$\frac{27.84}{31} = 0.90$	$\frac{35.40}{38} = 0.93$
wabs×(diskbb+po)	$\frac{17.53}{21} = 0.83$	$\frac{19.16}{22} = 0.87$	$\frac{26.10}{29} = 0.90$	$\frac{28.63}{36} = 0.80$
ftest probability	0.63	0.036	0.39	0.022
wabs×po ($N_{\rm H}$ fixed)	$\frac{20.02}{24} = 0.83$	$\frac{38.41}{25} = 1.54$	$\frac{36.82}{32} = 1.15$	$\frac{39.81}{39} = 1.02$
wabs×(diskbb+po) ($N_{\rm H}$ fixed)	$\frac{18.28}{22} = 0.83$	$\frac{22.27}{23} = 0.97$	$\frac{27.88}{30} = 0.93$	$\frac{32.85}{37} = 0.89$
ftest probability	0.37	0.002	0.015	0.038

Table 7. Fit results of Fig. 6.

	$kT_{\rm in} = N \times (L_{\rm disc}/(L_{\rm Edd} \times b))^{\alpha_1}$ when $L_{\rm disc}/L_{\rm Edd} > b$ $kT_{\rm in} = N \times (L_{\rm disc}/(L_{\rm Edd} \times b))^{\alpha_2}$ when $L_{\rm disc}/L_{\rm Edd} < b$					$kT_{\rm in} = N \times (L_{\rm disc}/L_{\rm Edd})^{\alpha_{\rm spl}}$
	b	N	α_1	α_2	$\chi^2_{\rm bknpl}/\nu$	$\chi^2_{\rm spl}/\nu$
$N_{\rm H}$ free	0.014 ± 0.001	0.46 ± 0.021	0.27 ± 0.018	0.77 ± 0.15	22.9/20	109.2/22
$N_{\rm H}$ fixed	0.014 ± 0.001	0.47 ± 0.016	0.26 ± 0.018	0.57 ± 0.1	46.04/20	214/22
	$R_{\rm in}/{\rm R_g} = {\rm N} \times ({\rm L_{bol}}/({\rm L_{Edd}} \times {\rm b}))^{\alpha_1}$ when $L_{\rm bol}/L_{\rm Edd} > b$ $R_{\rm in}/{\rm R_g} = {\rm N} \times ({\rm L_{bol}}/({\rm L_{Edd}} \times {\rm b}))^{\alpha_2}$ when $L_{\rm bol}/L_{\rm Edd} < b$					$R_{\rm in}/{\rm R_g} = {\rm N} \times ({\rm L_{bol}}/{\rm L_{Edd}})^{\alpha_{\rm spl}}$
	b	N	α_1	α_2	$\chi^2_{\rm bknpl}/\nu$	$\chi^2_{\rm spl}/\nu$
$N_{\rm H}$ free	0.015 ± 0.003	5.56 ± 0.32	-0.05 ± 0.03	-2.4 ± 1.4	55.8/20	152/22
$N_{\rm H}$ fixed	0.015 ± 0.002	5.20 ± 0.30	-0.02 ± 0.02	-1.72 ± 0.6	37.09/20	299/22
	$R_{\rm in}/{\rm R_g} = {\rm N} \times ({\rm kT_{in}}/{\rm b})^{\alpha_1}$ when $kT_{\rm in} > b$ $R_{\rm in}/{\rm R_g} = {\rm N} \times ({\rm kT_{in}}/{\rm b})^{\alpha_2}$ when $kT_{\rm in} < b$					$R_{\rm in}/{\rm R_g} = {\rm N} \times ({\rm kT_{in}})^{\alpha_{\rm spl}}$
	b	N	α_1	α_2	$\chi^2_{\rm bknpl}/\nu$	$\chi^2_{\rm spl}/\nu$
$N_{\rm H}$ free	0.44 ± 0.10	5.20 ± 0.60	-0.12 ± 0.15	-1.44 ± 0.7	82.7/20	107.34/22
$N_{\rm H}$ fixed	0.50 ± 0.03	4.96 ± 0.57	-0.02 ± 0.09	-0.99 ± 0.2	47.7/20	175.6/22

5 MULTI-SOURCES COMPARISONS

While XTE J1817-330 is one of the best-studied examples, we need to see how typical its behaviour is for BHBs. We first extended the previous study to the other available SWIFT data of candidate black holes, i.e GX 339-4, SWIFT J1753.5-0127 and GRO J1655-40. According to the results obtained in Sect. 3, we let the value of $N_{\rm H}$ free to vary and used an absorbed `powerlaw` (and a `diskbb` when needed) to model the spectra. Observations where a thermal component is required are plotted in Fig. 8.

Contrary to the case of XTE J1817-330, there is less systematic evolution of the disk radii. Indeed, if a faint increasing of its value seems to occur at low luminosity in GX 339-4, the statistics are not sufficient to draw any conclusions. The addition of the broadband analysis of lower luminosity states led by Tomsick et al. (2008) (T08) changes this a bit. Indeed, when using reflection models, T08 seem to obtain a geometry that does not evolve through the hard state (the solid angle value remains constant and high enough). On the contrary, the normalisation of the multicolour disc tends to exhibit quite high value, whatever the high energy model chosen. For purpose of simpler comparison between sources, we included the results coming from their modelling by a simple absorbed `diskbb+powerlaw`. Moreover, the evolution of the bolometric luminosity is small (changes by a factor of ~ 5 only) and thus further observations of the decline would be necessary. GRO J1655-40 exhibits unusual behaviour; although the fitted radii change by a factor of two, the relationship between the temperature and the disc luminosity is not monotonic but rather quite complex. SWIFT J1753.5-0127 even shows a disc that tends to get hotter when its luminosity decreases, with a higher internal radius in more luminous state. However, we were limited by the statistics and narrow range in luminosity sampled.

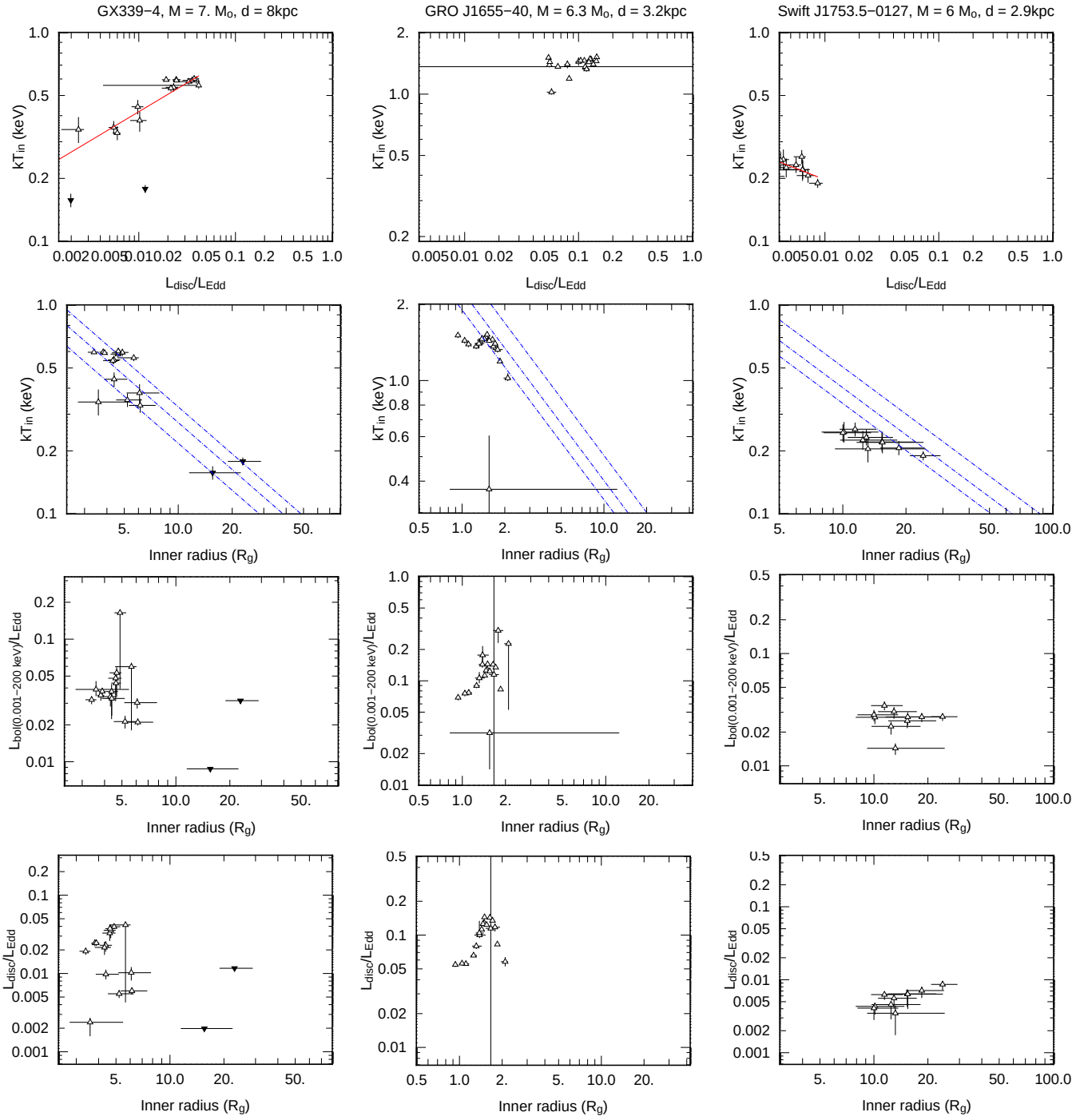

Figure 8. Variation of the disc properties of GX 339-4 (first column), GRO J1655-40 (second column) and SWIFT J1753.5-0127 (third column) as recorded by SWIFT. Note that in the case of GRO J1655-40, the source is in outburst whereas it is mainly in the decline for both others. On top left panel, fit of the cloud of point by a powerlaw gives an index of ~ 0.10. For SWIFT J1753.5-0127, this index is found to be negative (~ -0.21): the disc luminosity decrease when the temperature increase. Concerning the $kT_{\rm in}$ vs $R_{\rm in}$ plots, same coding in $\dot{m}_{\rm d}$ as in Fig. 6 has been used. For GX 339-4, both points corresponding to the observations analysed by T08 (▼ symbols) with a simple absorbed `diskbb+powerlaw` have been added.

We then compared the whole set of sources in a single study. This has been done by overplotting on the same graph the previous results, and adding the few points obtained at lower luminosities. These latter points mainly come from the low efficient BHB XTE J1118+480. However, other recent or older observations of the previous sources (T08 for GX 339-4 and S07 for XTE J1817-330 as mentioned before) have been added. The overall results are displayed in Figs. 9, 10, 11, 12, 13, 14 and 15.

Mass, distance and inclination angle uncertainties

The uncertainties plotted directly on the graphs are the statistical errors arising from the fits. We also attempted to estimate the systematic uncertainties due to the the orbital parameters (see Tab. 1). For simplification, we computed the lower and upper boundaries by taking the limit values in masses, distances and angles. For example, as the disc luminosity goes with $L_{\rm disc}/L_{\rm Edd} \propto F_{\rm disc} d^2/(M \times \cos(i))$, all the disc luminosities will be shifted by a factor $d^2_{\rm max}/(M_{\rm min} \times \cos(i_{\rm max}))$ if one wants to obtain the highest value of $L_{\rm disc}/L_{\rm Edd}$.

This corresponds to a vector in Fig. 9. We note, however, that this method is somewhat overestimating the shifts in the corresponding diagrams as there may be strong correlation among those parameters. As the mass is often determined via the mass function, in that case $M \times \sin^3(i)$ must remain constant when evaluating the uncertainties. In addition, since for the recently discovered black-hole candidates (J1817-330 and J1753.5-0127) there is no proper orbital measures yet, we have set quite large uncertainties.

5.1 Disc geometry evolution

We first investigate the global relation between the disc luminosity and its inner temperature (Fig. 9). As was pointed out in the previous sections, a constant truncation radius would mean a constant relationship with $T_{\rm in} \propto L_{\rm disc}^{0.25}$. We thus have drawn in Fig. 9 this relation, normalised to the temperatures obtained in the highest luminosity states of GX 339-4 and XTE J1817-330. An examination of the diagram shows that around $L_{\rm disc} \sim 10^{-2} L_{\rm Edd}$, the points seem to slightly deviate from this relationship toward the lower luminosities. If we then include the points at lower luminosities and in quiescence (mostly coming from XTE J1118+480), this deviation appears more clearly. The fact that the points are located below the relationship would thus indicate an increase of the multicolour disc normalisation $K_{\rm disc}$, hence the radius (normalised to R_g).

As pointed out in the previous paragraph, GRO J1655-40 (• points) exhibits a rather different behaviour as for the same disc (and even bolometric, see Fig. 10) luminosity, the inner temperature is higher in the highest states. This is more obvious when considering that their points are not located around the dashed relation in Fig. 9. The bias coming from the distance and the mass uncertainties could explain part of this discrepancy. However, as the disc luminosity should be about 10 times higher in order to fit this relation, it implies changes of a factor three in distances or a factor 10 in masses between sources (or some combination of the two). Another reasonable explanation could be that the truncation radius value in the highest states of GRO J1655-40 is closer to the horizon than in the other X-ray binaries studied, increasing its efficiency for an equivalent accretion rate. This may imply higher spin.

The apparent overall increase in radius when the luminosity decreases was then probed by the relation between the disc or bolometric luminosity (Figs. 10 and 11) and the inner temperature (Fig. 12) or the photon index (Fig. 13). When examining the disc luminosity as a function of the inner radius (Fig. 11), this trend seems to be confirmed with a few exceptions. Among them are some of the GX 339-4

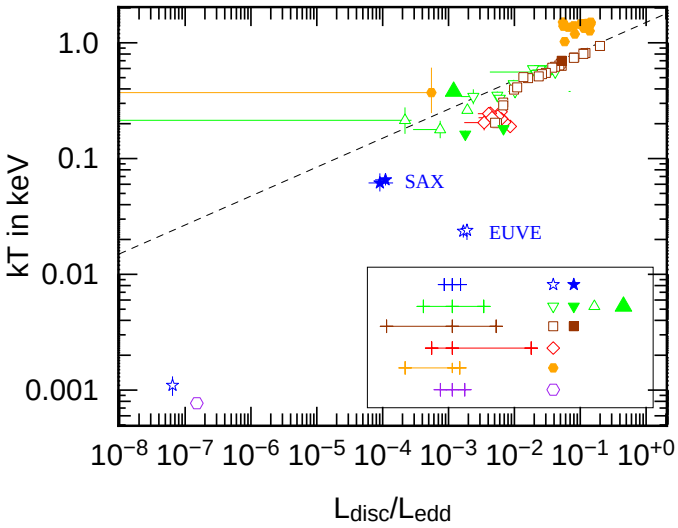

Figure 9. $kT_{\rm in}$ versus $L_{\rm disc}/L_{\rm Edd}$. The black dashed correspond to $T_{\rm in} \propto (L_{\rm disc}/L_{\rm Edd})^{0.25}$. The impact of the orbital parameters (distance, mass and inclination angle) uncertainties on the disc luminosity is shown on the inset for each source (see text for precisions). Colour/symbol code: GX 339-4 (▽: SWIFT data. ▼: T08. △: ASCA data. ▲: M06). GRO J1655-40 (●, SWIFT data). XTE J1817-330 (□: SWIFT data. ■: S07). SWIFT J1753.5-0127 (◇, SWIFT data). XTE J1118+480 (★. open : EUVE data. filled : SAX data). A0620-00 (○).

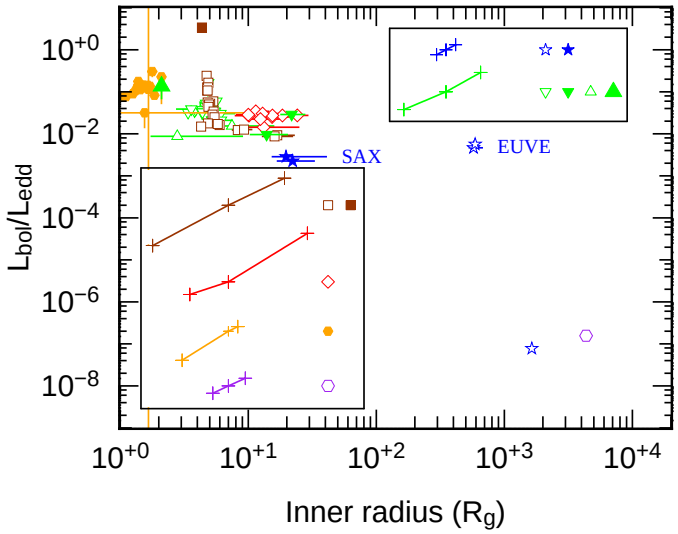

Figure 10. Inner radius versus $L_{\rm bol}/L_{\rm Edd}$. Shifts in radius and luminosities due to orbital parameters uncertainties are shown in the insets. Colour/symbol code is the same as in Fig. 9.

observations, and obviously the one observation from XMM by M06 (▲ point).

As pointed out by these authors, the radius value inferred by the thermal component is close to 2 R_g, even though the disc luminosity is very low ($L_{\rm disc} \sim 10^{-3} L_{\rm Edd}$), suggesting a non recessed disc even in the low accretion rate states. However, considering the bolometric luminosity (see e.g Fig. 10), we note a different behaviour. In that case we have $L_{\rm bol} \sim 1.4 \times 10^{-1} L_{\rm Edd}$. This suggests that the source was in quite a high state during this observation, even

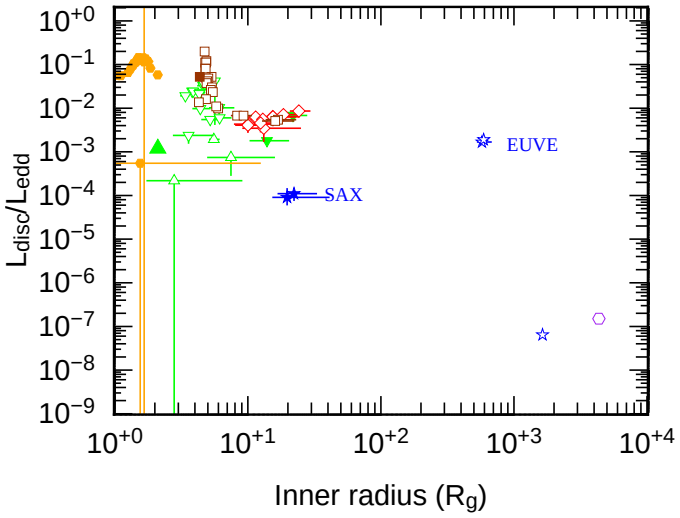

Figure 11. Evolution of the disc luminosities in function of the inferred internal radius between different sources.

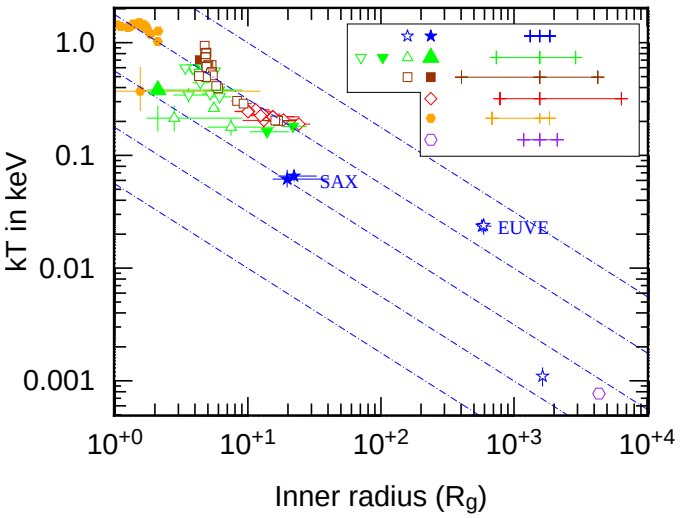

Figure 12. Inner radius versus temperature. Blue dotted-dashed lines : relationship obtained for a 8 $M_\odot$ BH accreting at constant $\dot{m}_{\rm d}$ and an Eddington efficiency $\eta = 0.1$. From upper right to lower left $\dot{m}_{\rm d} = 1, \times 10^{-2}, \times 10^{-4}, \times 10^{-6}, \times 10^{-8}$. Colour/symbol code is the same as in Fig. 9.

though being spectrally hard (as the photon index $\Gamma \sim 1.46$). Indeed, as shown in Fig. 10, and looking at whole data set, the evolution of $L_{\rm bol}$ vs $R_{\rm in}$ seems to be less discrepant and an increasing radius is consistent with $L_{\rm bol} \lesssim 10^{-2} L_{\rm Edd}$.

This is emphasised by the analysis of Fig. 12, as the inner radius values seem to roughly anti-correlate with the inner temperatures when $kT_{\rm in} \lesssim 0.5$ keV. The data seems to follow one of the dashed lines for the relation between $T_{\rm in}$ and $R_{\rm in}$ (Eq. 6) for a $8 M_\odot$ BH and a constant accretion rate in the disc, $\dot{m}_{\rm d}$.

However, by using (Eq. 7) and taking into account the different BH masses, we infer the evolution of the disc accretion rate $\dot{m}_{\rm d}$. As shown in Fig. 14, the disc accretion rate seems to roughly scale with the bolometric luminosity in the highest states, i.e $L_{\rm bol} > 10^{-2} L_{\rm Edd}$. The behaviour under this value is less clear. On the one hand, XTE J1817-330

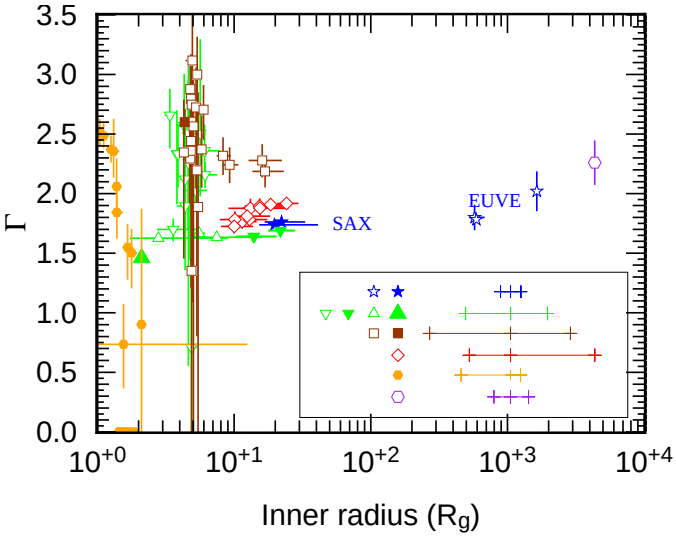

Figure 13. Photon index Γ vs the internal radius of the optically thick disc. Colour/symbol code is the same as in Fig. 9.

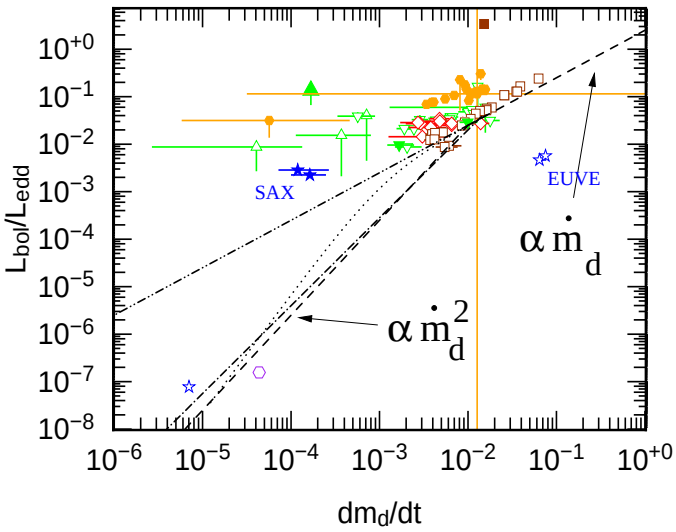

Figure 14. Bolometric luminosity as function of the accretion rate in the optically thick disc $\dot{m}_{\rm d}$ obtained for our sample, using equation 7. Points are subject to global horizontal shifts due to the actual Eddington efficiency value used. The set of curves shows theoretical relations. Dashed : $L_{\rm bol} \sim L_{\rm disc} \propto \dot{m}_{\rm d}$ when $R_{\rm in} = 6$ $R_{\rm g}$ and the efficiency at Eddington luminosity $\eta_{\rm Edd} = 0.1$. Under $\sim 10^{-2} L_{\rm Edd}$, continuing relationship when $L_{\rm bol} \propto \dot{m}_{\rm d}^2$. Supposing $\dot{m}_{\rm total} \sim \dot{m}_{\rm d}$ we have: ADAF solutions (dotted), MH02 (Dot-dot-dashed) and RC00 (Dot-dashed). The value of α and β are the same as in Fig. 16. Errors on $\dot{m}_{\rm d}$ were computed by propagating those on the temperature and the inner radius only. Colour/symbol code is the same as in Fig. 9.

seems to exhibit a beginning of rapid decay of the radiation efficiency ($L_{\rm bol}$ divided by a factor 2 for a rather constant $\dot{m}_{\rm d}$ between observation number 15 and 17). On the other hand, considering the whole data set at those low luminosities, the obvious lack of disc detections and the larger uncertainties are insufficient to draw the profile of $L_{\rm bol}$ as a function of $\dot{m}_{\rm d}$ with accuracy. It is however compatible with $L_{\rm bol}/L_{\rm Edd} \propto \dot{m}_{\rm d}^2$ by taking into account the sources observed

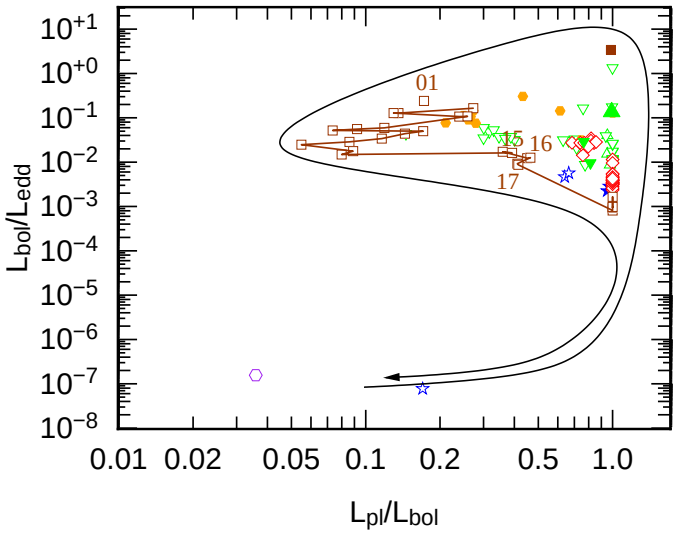

Figure 15. Disc fraction luminosity diagram of the whole set of observations presented in this paper. The arrow represent the supposed path in the DFLD during an outburst, starting from quiescence. Colour/symbol code are the same as in Fig. 9.

in quiescence. This corresponds to a scenario in which a receding, but radiatively efficient, outer disc feeds an inner, radiatively inefficient flow.

However, the canonical BHB states do not depend on luminosity (see e.g the classification scheme of McClintock & Remillard 2003b which is based on spectral, timing and radio behaviour or Homan & Belloni 2005). Therefore we plot the evolution of the inner radius as function of the photon index, Γ in Fig. 13. The evolution is then as follows. In the softest states, radii remain quite constant, as for example the average value obtained for XTE J1817-330 and GX 339-4 when $\Gamma > 2.4$ (14 observations) is $R_{\rm in,\ avg} = 4.91$ R_g, with a standard deviation of $\sigma_{R_{\rm in,\ rms}} = 0.59$ R_g. On the contrary, for lower photon indices, the data are compatible with an increase of the inner radius when the spectrum hardens, as long as quiescence is not reached. Indeed, in quiescence the photon index values are usually higher ($\Gamma \sim 2$). This effect was noted in other sources as well (e.g. in V404 Cyg $\Gamma \sim 2.1$, see Narayan et al. 1997).

Finally, we investigate the evolution of the relative strength of each component (i.e emission from the optically thick vs optically thin medium) during the outburst. "Hardness-Intensity Diagrams" (HID) are commonly used for such analysis because of their emission model independence (see e.g Belloni et al. 2004). However, they are not easily adapted to multi-instrument and multi-object analysis. Following the method used by Körding, Jester & Fender (2006), we use the so-called "Disc Fraction Luminosity Diagram" (DFLD) that aims at generalising the concept of HID: in HIDs harder states are located on the right of the diagram and correspond to higher powerlaw contribution. For better ressemblance, in DFLD we use on X axis the "Power law fraction" (PLF):

$$PLF = \frac{L_{\rm PL}}{L_{\rm disc} + L_{\rm PL}}, \qquad (8)$$

which describes well the disc contribution as the "Disc Fraction" (DF) is then in turn:

$$DF = 1 - PLF. \qquad (9)$$

The DFLD corresponding to our data set is plotted on Fig. 15. Of primary importance is first the pattern drawn by XTE J1817-330 during its decline. As the bolometric flux fades, the optically thick component is dominating and even seems to increase its contribution (PLF falls by a factor 2 between observation number three and 13). Then the PLF suddenly increases and this turnover corresponds to the observations (number 15, 16 and 17) where a recessed disc begins to appear. However, it is not accompanied by a drastic change in bolometric luminosity, suggesting that the inner part of the disc has been replaced by a quite efficient corona.

We also note that the powerlaw fraction value in quiescence is equivalent to that observed in the softest states. Therefore we suggest that the track followed by a BH X-ray binary should be roughly equivalent to the one plotted on Fig. 15 (black arrow). From quiescence, the source will progressively increase its PLF as it usually enters in outburst by its low-hard state. Then, the powerlaw fraction decreases due to the presence of the thermal component in the former "high-soft" state and finally returns to the hard and quiescent states.

However, this simple pattern is susceptible to be altered whenever a high intermediate state with a strong powerlaw component is present. In order to confirm this trend, further monitoring is therefore still necessary.

5.2 Comparison with timing semi-empirical relationship and accretion models

5.2.1 ADAF and inner disc evaporation models

Further investigations were then led to compare our results to available accretion models. Our goal is to constrain the mechanisms responsible for the optically thin and radiatively inefficient flows. For that purpose, we mainly used the models proposed by (Czerny, Rózańska & Kuraszkiewicz 2004, CRK04) as particular attention is paid to the evolution of inner disc radii. We compared our data to the following three models - the classical strong ADAF solutions (Abramowicz 1995 = "A" model), and two other models (Meyer & Meyer-Hofmeister 2002 = "B" model or "MH02" and Różańska & Czerny 2000 = "C" model or "RC00") where evaporation of the inner part of the cold disc is taken into account. In these latter models, the evaporation efficiency is driven by conduction between the corona and the disc in presence of a magnetic field.

We also identified the evaporation radius $R_{\rm evap}$ described in those papers with the internal radius we obtained from our fits ($R_{\rm evap} = R_{\rm in}$). As modeled by CRK04, one can then infer the dependency between $R_{\rm in}$ and $L_{\rm bol}$ simply by tuning the values of two parameters, the classical α viscosity parameter and the magnetisation $\beta = P_{\rm gas}/(P_{\rm mag} + P_{\rm gas})$ in the hot plasma.

We then used the equations given in CRK04 and briefly explored the (α, β) plane for models "A" and "C" (β plane only for model "B", as the analysis driven by Meyer & Meyer-Hofmeister was only computed with $\alpha = 0.3$). One constraint we assess is the values of the luminosity when the inner radius seems to begin to increase. We set

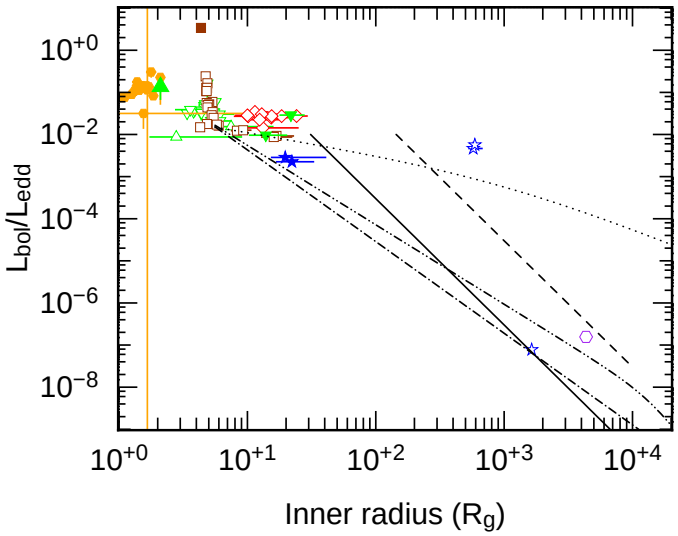

Figure 16. Same as Fig. 10 but with models overplotted. Continuous curve refers to the accretion model or timing relationship used (see text). Parameters value used: ADAF (dotted curve) $\alpha = 1.33 \times 10^{-2}$ and $\beta = 1.e-8$. MH02 (Dot-dashed curve): $\alpha = 0.3$ and $\beta = 0.11$. RC00 (Dot-dot-dashed): $\alpha = 3{\times}10^{-5}$ and $\beta = 0.11$. For the timing relationships, we use either $\nu_{\rm l} = \nu_{\rm Keplerian}(R_{\rm in})$ (dashed line) or $\nu_{\rm l} = \nu_{\rm sound}(R_{\rm in})$ with $h_{\rm d}/R_{\rm in} = 0.1$ (solid line). Colour/symbol code is the same as in Fig. 9.

this value arbitrarily to the one obtained with XTE J1817-330 (see Tab. 7), i.e $L_{\rm bol} \sim 0.015\ L_{\rm Edd}$ and $R_{\rm in} = 5.6\ {\rm R_g}$. Each model with an example of (α, β) values that fulfil this requirement was then overplotted on Fig. 16.

For the ADAF ("A") model, the adopted value for the viscosity parameter was $\alpha = 0.013$. As shown as well in Fig. 2 of CRK04, the radiative efficiency depends only slightly on the value of the magnetisation parameter in this case. Decreasing β only tends to deviate a little towards the lower luminosity the $L_{\rm bol}$ vs $R_{\rm in}$ curve for large values of the inner radius. As a result, even with such a low value as $\beta = 10^{-8}$ (i.e plasma highly magnetised) , the curvature does not allow the ADAF model to reproduce the very low luminosity observed in quiescence if the viscosity parameter α is the same between the highest and quiescent state (as shown on Fig. 16). Any attempt to fit the points in quiescence would require a value of $\alpha \sim 3 \times 10^{-4}$, however the state where the radius would begin to increase would then occur at $L_{\rm bol} \sim {\times}10^{-5} L_{\rm Edd}$. We note that the ADAF model fits well the beginning of the recession observed in XTE J1817-330. This model predicts indeed that

$$\frac{R_{\rm in}}{\rm R_g} \propto \alpha^4 \dot{m}^{-2}. \qquad (10)$$

Moreover, in the highest states, the accretion process still remains quite efficient, giving $L_{\rm bol}/L_{\rm Edd} \propto \dot{m}$ (see Eq. 16, 17 and 18 of CRK04 for further details). We therefore get:

$$\frac{R_{\rm in}}{\rm R_g} \propto \left(\frac{L_{\rm bol}}{L_{\rm Edd}}\right)^{-2}. \qquad (11)$$

It is interesting to note that this exponent value of -2 is consistent with that obtained when fitting by a broken powerlaw the $R_{\rm in}$ vs $L_{\rm bol}$ points for XTE J1817-330 (see Tab. 7 : $\alpha_2 = 2.4$ or 1.7). Moreover, when extended to larger radii, the ADAF solution seems to be in quite good agreement with the data obtained with EUVE for the XTE J1118+480 outburst as well.

Nevertheless, we have shown that the ADAF solutions do not seem to fit the $L_{\rm bol}$ vs $R_{\rm in}$ relationship in both high and quiescent states. On the other hand, the approximate relation giving the accretion radiative efficiency (equations 16, 17 and 18 of CRK04) seems to fit the data, as shown on Fig. 14 (dotted curve) and if we assume that $\dot{m}$ scales as $\dot{m}_{\rm d}$.

Compared to the ADAF model, the models where evaporation of the inner part of the disc is taken into account seem to be a better overall description of the $L_{\rm bol}$ vs $R_{\rm in}$ evolution. In these cases, the magnetisation value has far more impact. Taking $\beta = 0.11$ (i.e $P_{\rm mag} \sim 8 P_{\rm gas}$) with the MH02 model allows us to fit the overall shape of both the quiescent and the low state observations (except XTE J1118+480 EUVE data). A similar result can be obtained with RC00 model with a similar value of the magnetisation, but quite a lower value of the viscosity parameter ($\alpha = 3 \times 10^{-5}$). The main drawback concerning such a low value of α can be seen on Fig. 14 (dot-dot-dashed curve). The radiative efficiency does not drop at low $\dot{m}$ and the accretion flow remains radiatively efficient, inconsistent with the points in quiescence. No other (α, β) combination has been found which better mimics the behaviour in both $L_{\rm bol}$ vs $R_{\rm in}$ and $L_{\rm bol}$ vs $\dot{m}$ diagrams. This problem does not seem to occur with MH02 model (dot-dashed curve) where the value of $\alpha = 0.3$ is higher.

5.2.2 *Using the Variability Plane*

We subsequently tried to compare our spectral fitting results with the expected timing behaviour. Indeed, Mc Hardy et al. (2006) found that AGN and stellar soft state BH could be unified by taking the accretion rate and the BH mass into account. Indeed, a fundamental plane seems to link the typical frequency observed in the power spectra (especially to the lower high frequency Lorentzian $\nu_{\rm l}$), the BH mass (M) and the total accretion rate $\dot{m}$

$$\left(\frac{\nu_{\rm l}}{Hz}\right)\left(\frac{M}{10 M_\odot}\right) \propto \left(\frac{\dot{M}}{\dot{M}_{\rm Edd}}\right). \qquad (12)$$

Körding et al. (2007) found afterwhile that this relationship could be extended to hard states, even if the normalisation is not exactly the same, neither is the characteristic frequency (in soft state of BHB and AGN, it is the high frequency break). If typical frequency observed is linked to a Keplerian motion near the internal radius of the accretion disc $R_{\rm in}$, we get:

$$\nu_{\rm l} \propto (M)^{1/2} (R_{\rm in})^{-3/2} \propto (M)^{-1} \left(\frac{R_{\rm in}}{\rm R_g}\right)^{-3/2}, \qquad (13)$$

when normalising $R_{\rm in}$ to the gravitational radius ${\rm R_g} \propto {\rm M}$. Thus replacing $\nu_{\rm l}$ in equation 12 by the previous value gives:

$$(M)^{-1}\left(\frac{R_{\rm in}}{\rm R_g}\right)^{-3/2}(M)\propto\dot{m}\iff\dot{m}\propto\left(\frac{R_{\rm in}}{\rm R_g}\right)^{-3/2}. \quad (14)$$

For inefficient accretion flows that may occur at low luminosities, one can also have:

$$\frac{L_{\rm bol}}{L_{\rm Edd}}\propto\dot{m}^2, \quad (15)$$

whereas for efficient ones it is proportional to $\dot{m}$. We can thus infer a relationship between the internal radius of the standard accretion disc (normalised to $\rm R_g$) and the bolometric luminosity by combining Eqs. 14 and 15:

$$\frac{L_{\rm bol}}{L_{\rm Edd}}\propto\left(\frac{R_{\rm in}}{\rm R_g}\right)^{-3}, \quad (16)$$

in the inefficient case, whereas it goes as $(R_{\rm in}/\rm R_g)^{-3/2}$ when the flow is efficiently radiative.

The normalisation constant is actually undetermined in the relationship linking the radius and the typical frequency (Eq. 13), and is subject to variations in the other equations used. Hence we plotted the dependencies demonstrated in equation 16 on Fig. 16, using either the hypothesis that the frequency $\nu_{\rm l}$ used in Eq. 12 is exactly equal to the Keplerian frequency (Eq. 13, dashed line in Fig. 16), or to a sound wave. In this case, we have (see e.g. Czerny 2004, Eq. 3):

$$\nu_{\rm sound}=\left(\frac{h_d}{r}\right)\nu_{\rm Keplerian}. \quad (17)$$

This latter relationship implies that the normalisation in Eq. 16 is multiplied by a factor $(h_d/r)^2$. In Fig. 16, we plotted the corresponding relationship for $(h_d/r)=0.1$ (solid line), which seems to be more consistent with the points obtained by spectral fitting in the $10^{-8}-10^{-2}$ luminosity range.

6 DISCUSSIONS

6.1 Summary

In this paper we focused on the question of the evolution of the optically thick disc geometry during luminosity and state evolution observed in black hole binaries. Estimates of the internal radii values were obtained via modelling the thermal component in the spectra with a multicolour disc. In this simple model the luminosity is dominated by the internal part of the accretion disc that behaves like a blackbody of temperature $T_{\rm in}$ and surface $4\pi R_{\rm in}^2$.

However, as the optically thick disc in a BHB is usually emitting in the soft X-rays or far UV, the normalisation of this component is strongly dependant the value of the interstellar (and internal) absorption along the line of sight. We studied four sources to determine if there were possible changes in the value of $N_{\rm H}$ during state transitions. According to the data obtained with *Swift*, we demonstrated that when using a powerlaw for fitting the high energy component of the spectra, a decrease of the absorption is detected (above reasonable significance). This decreasing $N_{\rm H}$ is moreover observed when the source moves towards harder state. This effect is however not significant when using the thermal comptonisation model `comptt` (Titarchuk et al. 1994).

Taking this trend into account, we then studied the evolution of the disc geometry, firstly in the particular case of XTE J1817-330. We demonstrated that this source was indeed exhibiting the beginning of a disc recession. This was already noted by Gierliński, Done & Page (2008), but without taking into account disc irradiation, and contrary to what was stated by R07. This turnover in the disc behaviour is statistically significant (see Tab. 7), even when fixing the value of the hydrogen column density.

We then extended our study to a sample of six black hole binaries and tried to draw conclusions on the overall trend of the disc geometry evolution. These data, from a variety of instruments, are still consistent with a recession of the inner disc radius when the bolometric luminosity and the inner temperature decreases (see Fig. 10 and 12) or the spectrum hardens (Fig. 13).

Moreover in order to link the quiescent and high luminosity data, we also demonstrated that $L_{\rm bol}$ had to scale with the square of the accretion rate flowing through the optically thick disc $\dot{m}_{\rm d}^2$ (Fig. 14). Finally this evolution is consistent with accretion models where evaporation of the inner part of the disc is taken into account, however the strong ADAF hypothesis cannot be ruled out. The evolution of the disc radii values in function of the bolometric luminosity is also consistent with the expected behaviour derived from timing in the lowest accretion states (see Eq. 16). We therefore propose in Fig. 17 a general sketch displaying the evolution of BHB in function of their state and accretion rate.

6.2 Known limitations of the analysis

We only focused our analysis on the strength of the disc component in order to determine the disc geometry. Future investigations should correlate these results with those obtained either by iron line width fitting (but see hereafter the known limitations) or studies on the timing characteristics.

More importantly, we cannot exclude the possibility that the inner radii values obtained by using the simplistic multicolour disc model may sometimes be unphysical. Following e.g Sobczak et al. (2000), a sudden flare could result in an apparent decrease in the inner disc radius value when using the simple multicolour disc to fit the thermal component when no such decrease takes place in reality. This could be due to *increased spectral hardening and/or Compton upscattering of soft disk photons*, thus depleting the thermal component, and hence decreasing the observed radius value.

However, an increase in the radius when the source fades as observed in our study, seems more difficult to interpret in that framework. When moving towards the harder and lower states, one should on the contrary expect a decrease of the radius value, according to the previous reasons. Therefore if we had taken those effects into account, we would have even obtained bigger radii value during the transitions. This would lead to equivalent results as obtained by Gierliński, Done & Page (2008), who took into account the irradiation of the inner part of the disc by hard X-rays coming from the corona on the same XTE J1817-330 *Swift* data than ours. They concluded that instead of receding by

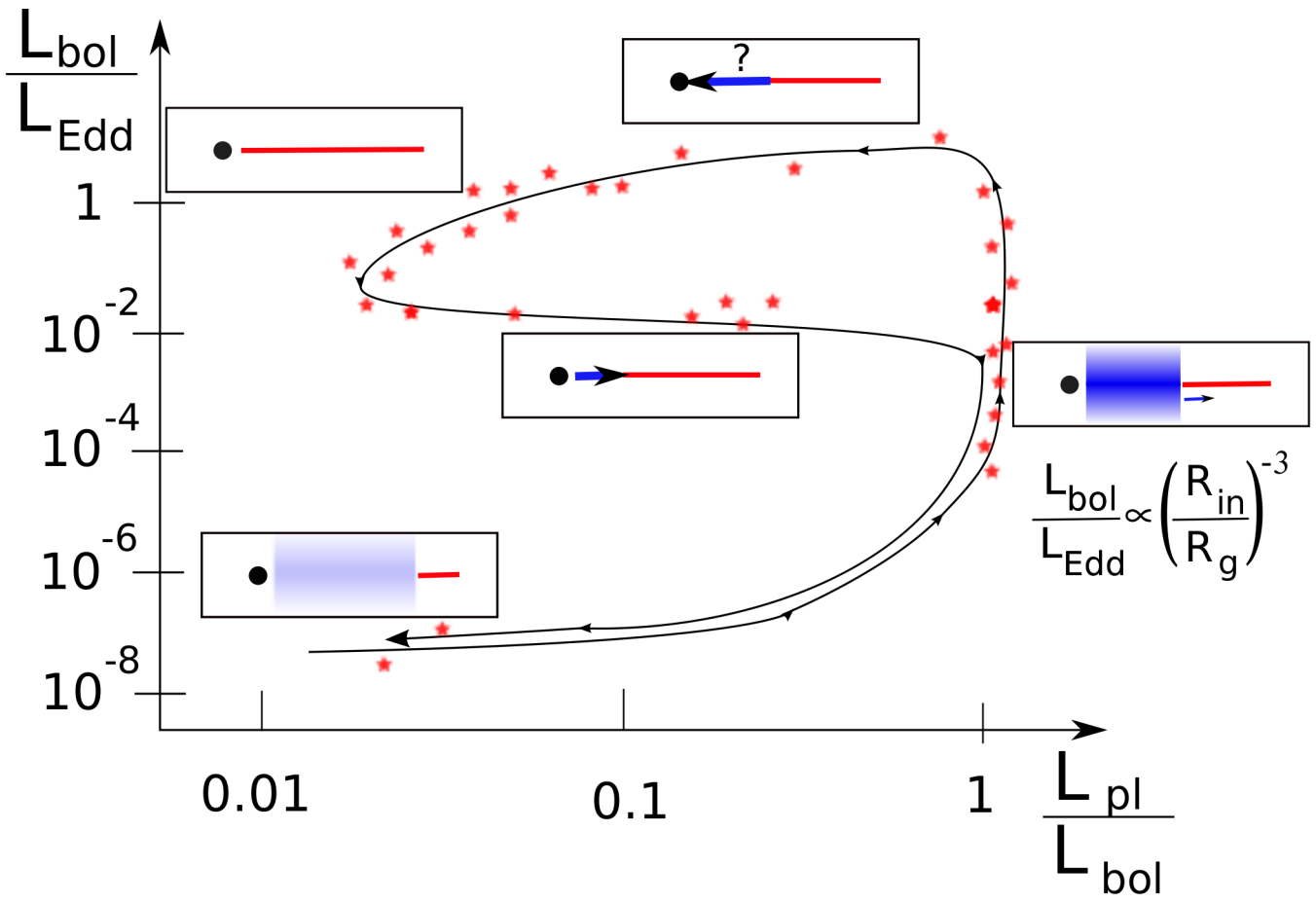

Figure 17. Expected behaviour of a BHB during outburst in the DFLD. Note that this general shape will not be valid if the source transit by a very high state (or "Steep Power Law") with a high contribution of the powerlaw component.

a factor two or three, as we obtained in this work, the inner radius would increase by a factor 6 to 8.

This irradiation model could therefore influence the relationship between $L_{\rm bol}$ and $R_{\rm in}$, and hence, the determination of the accretion models performed in Sect. 5.2.1 via a flattening of the actual relation. This model described in Gierliński, Done & Page (2008) depends mainly on one extra parameter, the ratio $R_{\rm c} = L_c/L_{\rm disc}$ (L_c being the comptonised component luminosity), which determines the deviation from the multicolour disc (see Fig. 6 of Gierliński, Done & Page 2008). The higher the $R_{\rm c}$ the more the deviation. As $R_{\rm c}$ can be linked to the value of the powerlaw/disc fraction PLF ($L_c \sim L_{\rm PL}$) giving $R_{\rm c} \sim PLF/(1-PLF)$, we can perform a rough estimate of the influence of irradiation on $R_{\rm in}$ in our study via the DFLD plotted in Fig. 15.

For XTE J1817-330, as in observations 15, 16 and 17, $PLF \sim 0.5$ and therefore $R_{\rm c} = 0.5$. Using Fig. 6 of Gierliński, Done & Page (2008), the radius should increase by a factor 1.25 only. This correction factor is negligible for points in higher states. The effect is however more striking for GX 339-4, SWIFT J1753.5-0127 and XTE J1118+480 in outburst. Indeed, both T08 data points have a $R_{\rm c} \sim 4$ and thus the radii obtained should then increased by a factor 3, giving $R_{\rm in} \sim 66$ and 42 $R_{\rm g}$. For SWIFT J1753.5-0.127, as $R_{\rm c}$ can reach values of 5, it would imply a correction factor of about 4. The case of XTE J1118+480 data obtained with Beppo-SAX is even more characteristic, as the luminosity is completely dominated by the optically thin component and $R_{\rm c} \sim 20$. As the lack of coverage in Fig. 6 of Gierliński, Done & Page (2008) does not allow us to infer the correction in radius, this implies, an increase by a factor five should be a minimum. Paradoxically, this could solve the discrepancy observed between radius values determined from Beppo-SAX and EUVE data. The EUVE data indicate that the correction factor in radius should not be higher than 2 ($R_{\rm c} \sim 2$). On the contrary, both quiescent points might be slightly affected by irradiation as in that case $R_{\rm c} < 0.2$. In any case, our study could be improved in the future by investigating the effect of adding irradiation, or reflection models to the fits (see e.g Reis et al. 2008 for a reanalysis of M06 data with reflection models, and Hiemstra et al. 2008 for the case of SWIFT J1753.5-0127 in the lowest states).

In addition to our extensive study, we note that an apparent disc recession during the decline was also noted in RXTE data at the end of the observations analysed by Sobczak et al. (2000) on XTE J1550-564 (the inner radius value rises by a factor three when the total flux drops by a factor 50).

The value of $R_{\rm in}$ obtained in quiescence can also be subject to systematic deviation, but for other reasons than those mentioned so far. As already pointed out by (MC03a),

the optical/UV excess observed in quiescence can also be mimicked by an ADAF, without requiring a disc, if we use the latest version of this model (Narayan et al. 1997). The value of the transition radius $R_{\rm tr}$ obtained by MC03a is then $\sim 10^4 R_{\rm S}$. As those latter authors do, we can hence reasonably estimate that in quiescence $2\times10^3 \leqslant R_{\rm in}/{\rm R_g} \leqslant 2\times10^4$.

Another problem arose from our study concerns the discrepancy observed in the outburst of XTE J1118+480 between Beppo-SAX and EUVE data. We already mentioned that disc irradiation could be one explanation, however it does not seem to be sufficient to account for the very large differences observed. Another possible explanation could come from the uncertainties in evaluating the extinction in EUVE data and thus the EUVE slope (see e.g Fig.3 of (MC01)), which could strongly affect the flux emitted by the source and hence the estimate of the radius. Independently to the discussions presented in (MC01) and (Ch03), we note that such a high radius from the EUVE data implies certain issues regarding the accretion efficiency. Fig. 15 shows that in order to account for the observed data, the accretion rate flowing through the disc must be quite high ($\dot{m}_{\rm d} \sim 0.1$). However, the low luminosity observed would also imply very inefficient flow, which is quite unusual compared to what is observed in the other BH binaries for such accretion rate.

We note however that the case of XTE 1118+480 in its 2000 outburst has recently been revisited by Reis et al. (2009). These authors base their analysis on Chandra and RXTE data alone and conclude that a non recessed disc is present, attributing the soft excess observed in EUV and radio to the synchrotron component of the jet. However the handling of the absorption in this study seems puzzling. In the final fits, the value of the absorption seems to stick at its higher boundary (fixed at 1.3×10^{20} cm^{-2}). We note furthermore that when it is allowed to vary more freely, its final value is quite higher ($\sim 2.7 \times 10^{20}$ cm^{-2}).

6.3 Consequences of a truncated/non truncated disc

Assuming we state that the overall trend of the optically thick disc is to exhibit a progressive recession of its inner radius, how can we interpret the recent observations of GX 339-4 (M06) and SWIFT J1753.5-0127 (Miller et al. 2006b)? First, as stated by those authors themselves, it can be peculiar case, or perhaps observations performed when the source was not steady. We cannot exclude, due to the long duration of the observation that the state could be a "mix" of a source transiting from the low to the high state for GX 339-4 for example.

Regarding the GX 339-4 observations from (M06) in detail, several points seems interesting to investigate. As we demonstrated (in Fig. 10), the bolometric luminosity is high ($\sim 0.1\ L_{\rm Edd}$) though with a low disc contribution. Hence, following Gierliński, Done & Page (2008), a complete treatment with the irradiation taken into account could give quite higher value to the inner radius observed as the powerlaw flux is completely dominating ($R_{\rm c} \sim 112$). Independently from this, the results obtained by the iron line fit with the `laor` model gives a very low inclination angle, $i = 18^{\rm o}$. Thus, if the inner disc and the orbit of the secondary are coplanar, as the mass function is $f_M = M_1 \sin^3(i)/(1 + M_2/M_1)^2 = 5.8 \pm 0.5$ (Hynes et al. 2003, where M_1: BH mass and M_2: secondary mass), this would imply a black hole mass of $M_1 \sim 200{\rm M}_\odot$ (for $M_2 = 1{\rm M}_\odot$) or $M_1 \sim 215{\rm M}_\odot$ (for $M_2 = 10{\rm M}_\odot$). These values are quite unusual for an X-ray transient, and the only way to disentangle this is to suppose the presence of a warped disc in GX 339-4 (see e.g Fragile, Mathews & Wilson 2001 for possible evidences in GRO J1655-40, or Maccarone 2002 for a more extensive study).

The case of SWIFT J1753.5-0127 in Miller et al. (2006b) is more subtle, even if as in GX 339-4, the powerlaw flux is dominating ($R_{\rm c} \sim 18$) and thus the irradiation could have an effect on the evaluation of $R_{\rm in}$. However, if the luminosity is quite low in Miller et al. (2006b), it mostly relies on the values of the mass and the distance of the source, which are currently not well known. If, we choose the values of our study (see Tab. 1), we obtain $L_{\rm bol}/L_{\rm Edd} \sim 1.5\times10^{-3}$. However, if $d = 8.5$ kpc, $L_{\rm bol}$ is nearly an order of magnitude higher.

We can also note that the addition of a reflection component on the disc (such as in Reis et al. 2008 or Hiemstra et al. 2008) could also explain part of the soft X-ray emission, and thus could decrease the disc intensity and the inner radius value inferred from the fits.

More fundamentally, a non truncated disc in the lowest state could raise some issues according to Dubus, Hameury & Lasota (2001) simulations. When a disc is present near the ISCO, instabilities in the disc seems to be unavoidable and a truncated disc prevents the triggering of such outbursts.

Finally, if we extend this study to larger scales, some data can also be obtained in the gap between 10^{-3} and $10^{-4}\ L_{\rm Edd}$ thanks to X-ray-Bright Optically Normal Galaxy (XBONG) and low luminosity AGN (M81, NGC 4579) data. Indeed, following Yuan & Narayan (2004), the corresponding inner radius obtained are close to $R_{\rm in} \sim 10^2$ R$_{\rm g}$ at $L_{\rm bol} \sim 10^{-4} L_{\rm Edd}$. Of importance, Fig. 3 of Yuan & Narayan (2004) seems indeed to exhibit roughly the same $L_{\rm bol}$ vs $R_{\rm in}$ relationship we obtain in Fig. 16, the corresponding "quiescent AGN" being Sgr A* and M87.

7 CONCLUSIONS

Based on several datasets obtained with instruments sensitive at low X-ray-energies (SAX, Swift, EUVE), we studied the optically thick component in BHB spectra and its evolution during outbursts via its contribution in the soft X-ray spectra. Any possible degeneracy with other processes such as the absorption in the line of sight was analysed. Depending on the nature of the high energy emission process, a possible variation of the hydrogen column density during outbursts is detected.

As a result of the good coverage by *Swift*, the case of XTE J1817-330 is examined in detail. Whereas for high bolometric luminosities ($> 10^{-2}$ L$_{\rm Edd}$) the inferred inner radius remains fairly constant, a sudden increase of its value is significantly detected when the luminosity is low ($< 10^{-2}$ L$_{\rm Edd}$). When including results coming from other sources and in quiescence as well, the hypothesis of a beginning of disc recession under $10^{-2} - 10^{-3}$ L$_{\rm Edd}$ is still favoured. The ob-

served disc recession rate with luminosity is also consistent with X-ray timing behaviour of BHs.

ACKNOWLEDGMENTS

CC thanks J. Malzac, G. Dubus, T. Maccarone, S. Chaty, I. Papadakis, P-O Petrucci, C. Done and the anonymous referee for their useful comments and discussions. This research has been funded in part by a Philip Leverhulme Prize awarded by the Leverhulme Foundation to RPF. RJHD acknowledges support from the Alexander von Humboldt Stiftung/Foundation. EGK acknowledges funding via a Marie Curie Intra-European Fellowship under contract no. MEIF-CT-2006-024668. This research was supported by the DFG cluster of excellence Origin and Structure of the Universe (www.universe-cluster.de).

REFERENCES

Abramowicz, M. A., Chen, X., Kato, S., Lasota, J.-P. and Regev, O., 1995, ApJ, 438, 37
Arnaud, K. A., 1996, ASPC, 101, 17A
Belloni, T., Mendez, M., King, A. R., van der Klis, M., van Paradijs, J., 1997, ApJ, 479L, 145B
Belloni, T., 2004, Nucl. Phys. B: Proc. Suppl., 132,337
Blandford, R. D. and Begelman, M. C., 1999, MNRAS, 303, L1
Boella, G., Chiappetti, L., Conti, G., Cusumano, G., del Sordo, S., La Rosa, G., Maccarone, M. C., Mineo, T., Molendi, S., Re, S., Sacco, B., Tripiciano, M., 1997, A&AS, 122, 327B
Brocksopp, C., McGowan, K. E., Krimm, H., Godet, O., Roming, P., Mason, K. O., Gehrels, N., Still, M., Page, K., Moretti, A., Shrader, C. R., Campana, S., Kennea, J., 2006, MNRAS, 365, 1203
Campana, S., Beardmore, A. P., Cusumano, G., Godet, O., 2007, `http://heasarc.nasa.gov/docs/heasarc/caldb/swift/docs/xrt/SWIFT-XRT-CALDB-09b_v2.pdf`
Chaty, S., Haswell, C. A., Malzac, J., Hynes, R. I., Shrader, C. R., Cui, W., 2003, MNRAS, 346, 689C (Ch03)
Coe, M. J., Engel, A. R. and Quenby, J. J., 1976, Nature, 259, 544
Cowley, A. P., Schmidtke, P. C., Hutchings, J. B., Crampton, D., 2002, AJ, 123, 1741
Cusumano, G, Campana, S, Moretti, A, 2005, `http://heasarc.nasa.gov/docs/heasarc/caldb/swift/docs/xrt/XRT-OAB-CAL_ARF_v3.pdf`
Czerny, B., Rózańska, A., Kuraszkiewicz, J., 2004a, A&A, 428, 39 (CRK04)
Czerny, B., 2004b, `astroph/0409254`
Dubus, G., Hameury, J.-M. and Lasota, J.-P., 2001, A&A, 373, 251
Esin, A. A., 1997, ApJ, 482, 400
Fender, R., Corbel, S., Tzioumis, T., McIntyre, V., Campbell-Wilson, D., Nowak, M., Sood, R., Hunstead, R., Harmon, A., Durouchoux, P. and Heindl, W., 1999, 519, L165
Fender, R. and Belloni, T., 2004, ARA&A, 42, 317
Fender, R. P. and Belloni, T. M. and Gallo, E., 2004, MNRAS, 355, 1105
Ferreira, J., Petrucci, P.-O., Henri, G., Saugé, L. and Pelletier, G., 2006, A&A, 447, 813
Foellmi, C., Depagne, E., Dall, T. H., Mirabel, I. F., 2006, A&A, 457, 249F
Fragile, P. C. and Mathews, G. J. and Wilson, J. R., 2001, ApJ, 553, 955
Frontera, F., Costa, E., dal Fiume, D., Feroci, M., Nicastro, L., Orlandini, M., Palazzi, E. and Zavattini, G., 1997, A&AS, 122, 357F
Frontera, F., Zdziarski, A. A., Amati, L., Mikołajewska, J., Belloni, T., Del Sordo, S., Haardt, F., Kuulkers, E., Masetti, N., Orlandini, M., Palazzi, E., Parmar, A. N., Remillard, R. A., Santangelo, A., Stella, L., 2001, ApJ, 561, 1006
Frontera, F., Amati, L., Zdziarski, A. A., Belloni, T., Del Sordo, S., Masetti, N., Orlandini, M., Palazzi, E., 2003, ApJ, 592, 1110
Gelino, Dawn M., Harrison, Thomas E., Orosz, Jerome A, 2001, AJ, 122, 2668G
Gelino, D. M., Balman, Ş., Kızıloğlu, Ü., Yılmaz, A., Kalemci, E. and Tomsick, J. A., ApJ, 2006, 642, 438
Gierliński, M. and Done, C., 2004, MNRAS, 347, 885
Gierliński, M., Done, C., Page, K., 2008, MNRAS, 388, 753
Gies, D. R., Bolton, C. T., 1986, ApJ, 304, 371G
Greene, J., Bailyn, C. D. and Orosz, J. A., 2001, ApJ, 554, 1290G
Homan, J. and Belloni, T., 2005, Ap&SS, 300, 107H
Hjellming, R. M., Rupen, M. P., 1995, Nature, 375, 454H,
Hiemstra, B., Soleri, P., Méndez, M., Belloni, T., Mostafa, R. and Wijnands, R., 2008, submitted to MNRAS
Hynes, R. I., Steeghs, D., Casares, J., Charles, P. A., O'Brien, K., ApJ, 583L, 95H
Körding, E. G., Jester, S. and Fender, R., 2006, MNRAS, 372, 1366
Körding, E. G., Migliari, S., Fender, R., Belloni, T., Knigge, C., McHardy, I., 2007, MNRAS, 380, 301
Maccarone, T. J., 2002, MNRAS, 336, 1371
Machida, M. and Nakamura, K. E. and Matsumoto, R., 2006, PASJ, 58, 193
Massey, P., Johnson, K. E., Degioia-Eastwood, K., 1995, ApJ, 454, 151
McClintock, Jeffrey E., Horne, Keith, Remillard, Ronald A., 1995, ApJ, 442, 358
McClintock, Jeffrey E., Remillard, Ronald A., 2000, ApJ, 531, 956
McClintock, J. E., Haswell, C. A., Garcia, M. R., Drake, J. J., Hynes, R. I., Marshall, H. L., Muno, M. P., Chaty, S., Garnavich, P. M., Groot, P. J., Lewin, W. H. G., Mauche, C. W., Miller, J. M., Pooley, G. G., Shrader, C. R., Vrtilek, S. D., 2001, ApJ, 555, 477M (MC01)
McClintock, J. E., Narayan, R., Garcia, M. R., Orosz, J. A., Remillard, R. A., Murray, S. S., 2003a, ApJ, 593, 435M (MC03a)
McClintock, J. E. and Remillard, R. A., 2003b, `astro-ph/0306213`
McConnell, M. L., Zdziarski, A. A., Bennett, K., Bloemen, H., Collmar, W., Hermsen, W., Kuiper, L., Paciesas, W., Phlips, B. F., Poutanen, J., Ryan, J. M., Schnfelder, V., Steinle, H. and Strong, A. W., 2002, ApJ, 572, 984
Mc Hardy, , I. M., Koerding, E., Knigge, C., Uttley, P., Fender, R. P., 2006, Nature, 444, 730
Meyer, F. and Meyer-Hofmeister, E., 2002, A&A, 392, L5,

(MH02)
Miller, J. M., Homan, J., Steeghs, D., Rupen, M., Hunstead, R. W., Wijnands, R., Charles, P. A., Fabian, A. C., 2006a, ApJ, 653, 525 (M06)
Miller, J. M., Homan, J. and Miniutti, G., 2006b, ApJ, 652, 113
Miller, J. M., Homan, J., Steeghs, D., Wijnands, R., 2006c, The Astronomer's Telegram, 746
Mineo, T., Romano, P., Mangano, V., Moretti, A., Cusumano, G., La Parola, V., Troja, E., Campana, S., Chincarini, G., Tagliaferri, G., Capalbi, M., Perri, M., Giommi, P., Burrows, D., 2007, astro-ph/0701815
Mitsuda, K., Inoue, H., Koyama, K., Makishima, K., Matsuoka, M., Ogawara, Y., Suzuki, K., Tanaka, Y., Shibazaki, N., Hirano, T., 1984, PASJ, 36, 741M
Narayan, R., Barret, D., McClintock, J. E, 1997, ApJ, 482, 448
Oosterbroek, T., van der Klis, M., Vaughan, B., van Paradijs, J., Rutledge, R., Lewin, W. H. G., Tanaka, Y., Nagase, F., Dotani, T., Mitsuda, K., Yoshida, K., 1996, A&A, 309, 7810
Parmar, A. N., Martin, D. D. E., Bavdaz, M., Favata, F., Kuulkers, E., Vacanti, G., Lammers, U., Peacock, A. and Taylor, B. G., 1997, A&AS, 122, 309P
Press, W. H., Teukolsky, S. A., Vetterling, W. T. and Flannery, B. P., 1992, Cambridge: University Press, —c1992, 2nd ed.
Protassov, R., van Dyk, D. A., Connors, A., Kashyap, V. L., Siemiginowska, A., 2002, ApJ, 571, 549
Reis, R. C., Fabian, A. C., Ross, R. R., Miniutti, G., Miller, J. M. and Reynolds, C., 2008, MNRAS,387, 1489
Reis, R. C., Miller, J. M., Fabian, A. C., 2009, `astroph/0902.2793v1`
Różańska, A. and Czerny, B., 2000, A&A, 360, 1170, (RC00)
Rykoff E. S. , Miller J. M, Steeghs D, Torres M. A. P, 2007, ApJ, 666, 1129 (R07)
Sala, G., Greiner, J., Ajello, M., Bottacini, E., Haberl, F., 2007, A&A, 473, 561 (S07)
Sobczak, G. J., McClintock, J. E., Remillard, R. A., Cui, W., Levine, A. M., Morgan, E. H., Orosz, J. A. and Bailyn, C. D., 2000, ApJ, 544, 993
Tananbaum, H., Gursky, H., Kellogg, E., Giacconi, R. and Jones, C., 1972, ApJ, 177, L5
Tauris, T. M. and van den Heuvel, E., 2003, `astro-ph/0303456`
Titarchuk, L, 1994, ApJ, 434, 313
Tomsick, John A., Kalemci, Emrah, Kaaret, Philip, Markoff, Sera, Corbel, Stephane, Migliari, Simone, Fender, Rob, Bailyn, Charles, Buxton, Michelle, `astroph/0802.3357`. (T08)
Van der Hooft, F., Heemskerk, M. H. M., Alberts, F., van Paradijs, J., 1998, A&A, 329, 538V
Van der Klis, M., 2001, ApJ, 561, 943
Wilms, J, Nowak, M. A., Dove, J. B., Fender, R. P. and di Matteo, T., 1999, ApJ, 522, 460W
Yuan, F. and Narayan, R., 2004, ApJ, 612, 724
Zdziarski, A. A., Poutanen, J., Mikolajewska, J., Gierlinski, M., Ebisawa, K., Johnson, W. N., 1998, MNRAS, 301, 435Z
Zdziarski, A. A., Gierliński, M., Mikołajewska, J., Wardziński, G., Smith, D. M., Harmon, B. A., Kitamoto, S., 2004, MNRAS, 351, 791

This paper has been typeset from a TEX/ LATEX file prepared by the author.

Table A. Table of the relevant fit/literature results we used in this study. The column densities values are expressed in 10^{22} cm^{-2}, $kT_{\rm in}$ in keV, $K_{\rm disc}$ in $10^3 \times (\mathrm{R_{in,\ km}/d_{10\ kpc}})^2 \cos(\mathrm{i})$, and the fluxes in terms of 10^{-10} erg.cm^{-2}.s^{-1}. The powerlaw flux values in parenthesis were not taken into account as the photon indices values obtained are irrealistic. Absorbed powerlaw fluxes are computed between 0.05 and 200 keV where unabsorbed disc fluxes are computed on the whole electromagnetic spectrum. Values written in italics are fixed during the fitting process.

Telescope	ObsId/Ref	$N_{\rm H}$	$kT_{\rm in}$	$K_{\rm disc}$	$F_{\rm disc}$	Γ	$F_{\rm PL}$	χ^2/ν
				XTE J1817-330				
Swift-XRT	00030367001	$0.165^{+0.026}_{-0.025}$	$0.939^{+0.014}_{-0.014}$	$2.25^{+0.18}_{-0.15}$	$378.5^{+18.7}_{-15.0}$	$2.31^{+0.27}_{-0.39}$	$79.14^{+17.32}_{-67.99}$	577.8/542
Swift-XRT	00030367002	$0.117^{+0.003}_{-0.003}$	$0.849^{+0.005}_{-0.005}$	$2.12^{+0.06}_{-0.06}$	$239.1^{+1.9}_{-1.3}$	–	–	623.7/536
Swift-XRT	00030367002	$0.128^{+0.055}_{-0.006}$	$0.815^{+0.007}_{-0.013}$	$2.39^{+0.11}_{-0.27}$	$227.9^{+21.3}_{-17.4}$	$1.35^{+1.33}_{-1.90}$	$85.81^{+0.00}_{-85.81}$	407.4/451
Swift-XRT	00030367003	$0.195^{+0.031}_{-0.029}$	$0.807^{+0.010}_{-0.010}$	$2.29^{+0.12}_{-0.12}$	$210.0^{+6.7}_{-6.6}$	$2.88^{+0.27}_{-0.28}$	$33.12^{+5.92}_{-9.52}$	432.7/461
Swift-XRT	00030367003	$0.171^{+0.031}_{-0.031}$	$0.802^{+0.010}_{-0.010}$	$2.37^{+0.14}_{-0.13}$	$211.7^{+7.1}_{-6.7}$	$2.60^{+0.29}_{-0.46}$	$31.70^{+6.07}_{-13.21}$	481.1/480
Swift-XRT	00030367004	$0.155^{+0.020}_{-0.019}$	$0.747^{+0.009}_{-0.008}$	$2.30^{+0.14}_{-0.14}$	$154.3^{+6.3}_{-6.8}$	$2.29^{+0.18}_{-0.23}$	$48.76^{+4.06}_{-6.67}$	521.4/518
Swift-XRT	00030367005	$0.175^{+0.025}_{-0.025}$	$0.741^{+0.012}_{-0.011}$	$2.33^{+0.21}_{-0.20}$	$152.0^{+7.2}_{-8.5}$	$2.36^{+0.20}_{-0.28}$	$53.22^{+5.40}_{-6.27}$	463.7/480
Swift-XRT	00030367006	$0.123^{+0.030}_{-0.015}$	$0.633^{+0.010}_{-0.009}$	$2.86^{+0.17}_{-0.16}$	$99.3^{+1.3}_{-0.0}$	$2.20^{+0.47}_{-1.39}$	$13.47^{+0.00}_{-13.47}$	368.1/396
Swift-XRT	00030367007	$0.160^{+0.048}_{-0.032}$	$0.661^{+0.009}_{-0.009}$	$2.34^{+0.12}_{-0.11}$	$96.2^{+2.8}_{-2.8}$	$2.80^{+0.37}_{-0.62}$	$9.82^{+0.35}_{-0.06}$	350.9/390
Swift-XRT	00030367008	$0.126^{+0.035}_{-0.023}$	$0.638^{+0.016}_{-0.009}$	$2.55^{+0.14}_{-0.13}$	$91.3^{+3.0}_{-2.6}$	$2.56^{+0.44}_{-2.56}$	$7.28^{+2.17}_{-7.28}$	347.4/368
Swift-XRT	00030367009	$0.205^{+0.098}_{-0.092}$	$0.620^{+0.023}_{-0.018}$	$2.46^{+0.36}_{-0.48}$	$78.8^{+6.0}_{-6.0}$	$3.12^{+0.63}_{-2.02}$	$16.32^{+0.00}_{-6.03}$	232.3/261
Swift-XRT	00030367009	$0.154^{+0.043}_{-0.042}$	$0.609^{+0.012}_{-0.012}$	$2.40^{+0.21}_{-0.19}$	$71.5^{+4.1}_{-3.5}$	$2.75^{+0.36}_{-0.83}$	$12.09^{+0.00}_{-1.29}$	305.8/324
Swift-XRT	00030367010	$0.166^{+0.042}_{-0.036}$	$0.550^{+0.008}_{-0.007}$	$2.89^{+0.15}_{-0.14}$	$57.1^{+1.2}_{-1.5}$	$3.00^{+0.31}_{-0.50}$	$7.54^{+1.67}_{-2.53}$	380.9/364
Swift-XRT	00030367011	$0.134^{+0.028}_{-0.022}$	$0.536^{+0.008}_{-0.008}$	$2.79^{+0.16}_{-0.15}$	$49.8^{+1.3}_{-1.3}$	$2.72^{+0.33}_{-0.68}$	$4.71^{+1.75}_{-4.71}$	351.8/350
Swift-XRT	00030367012	$0.108^{+0.021}_{-0.006}$	$0.512^{+0.009}_{-0.008}$	$2.99^{+0.18}_{-0.19}$	$44.5^{+1.4}_{-1.8}$	$1.89^{+0.96}_{-2.57}$	$2.60^{+1.77}_{-2.60}$	330.1/317
Swift-XRT	00030367013	$0.122^{+0.037}_{-0.017}$	$0.495^{+0.012}_{-0.012}$	$2.36^{+0.22}_{-0.19}$	$30.7^{+2.0}_{-1.5}$	$2.44^{+0.54}_{-1.22}$	$3.01^{+1.74}_{-3.01}$	273.9/273
Swift-XRT	00030367013	$0.114^{+0.021}_{-0.012}$	$0.505^{+0.009}_{-0.009}$	$1.84^{+0.13}_{-0.12}$	$26.0^{+1.1}_{-1.3}$	$2.35^{+0.44}_{-0.89}$	$2.27^{+0.71}_{-2.27}$	309.9/310
Swift-XRT	00030367015	$0.190^{+0.029}_{-0.029}$	$0.394^{+0.013}_{-0.013}$	$3.59^{+0.57}_{-0.61}$	$18.8^{+2.2}_{-2.1}$	$2.70^{+0.20}_{-0.25}$	$12.12^{+0.65}_{-1.10}$	301.1/328
Swift-XRT	00030367015	$0.153^{+0.031}_{-0.024}$	$0.412^{+0.017}_{-0.017}$	$3.36^{+0.52}_{-0.44}$	$20.9^{+2.4}_{-2.2}$	$2.37^{+0.28}_{-0.31}$	$11.76^{+0.74}_{-0.95}$	320.5/290
Swift-XRT	00030367016	$0.137^{+0.015}_{-0.014}$	$0.304^{+0.015}_{-0.016}$	$6.91^{+1.69}_{-1.23}$	$12.8^{+0.8}_{-1.1}$	$2.32^{+0.15}_{-0.15}$	$10.59^{+0.00}_{-0.47}$	304.1/321
Swift-XRT	00030367016	$0.147^{+0.014}_{-0.013}$	$0.288^{+0.016}_{-0.016}$	$8.64^{+2.48}_{-1.75}$	$12.8^{+1.0}_{-1.1}$	$2.24^{+0.14}_{-0.15}$	$11.19^{+0.92}_{-0.76}$	279.6/316
Swift-XRT	00030367017	$0.150^{+0.019}_{-0.017}$	$0.202^{+0.017}_{-0.017}$	$28.52^{+20.07}_{-10.36}$	$10.3^{+0.0}_{-0.2}$	$2.19^{+0.13}_{-0.13}$	$7.26^{+0.92}_{-0.66}$	241.3/247
Swift-XRT	00030367017	$0.151^{+0.020}_{-0.018}$	$0.204^{+0.019}_{-0.018}$	$25.88^{+19.35}_{-9.97}$	$9.7^{+0.2}_{-0.0}$	$2.28^{+0.13}_{-0.13}$	$6.91^{+0.56}_{-0.62}$	265.2/234
Swift-XRT	00030367019	$0.073^{+0.061}_{-0.055}$	–	–	–	$1.74^{+0.22}_{-0.20}$	$1.55^{+0.00}_{-0.44}$	18.3/23
Swift-XRT	00030367020	$0.005^{+0.050}_{-0.005}$	–	–	–	$1.73^{+0.25}_{-0.11}$	$3.15^{+3.07}_{-1.23}$	25.9/24
Swift-XRT	00030367021	$0.035^{+0.044}_{-0.035}$	–	–	–	$1.72^{+0.20}_{-0.19}$	$1.81^{+1.05}_{-0.55}$	27.8/31
Swift-XRT	00030367022	$0.069^{+0.039}_{-0.036}$	–	–	–	$2.28^{+0.22}_{-0.20}$	$1.87^{+0.60}_{-0.32}$	35.4/38
XMM	(S07)	$0.23^{+0.01}_{-0.01}$	$0.70^{+0.01}_{-0.01}$	$1.90^{+0.05}_{-0.05}$	99.45	$2.6^{+0.1}_{-0.1}$	6571.9	7536.25/6029
				SWIFT J1753.5-0127				
Swift-XRT	00030090001	$0.261^{+0.036}_{-0.030}$	$0.204^{+0.033}_{-0.028}$	$81.04^{+141.77}_{-48.75}$	$30.6^{+8.0}_{-15.1}$	$1.88^{+0.07}_{-0.08}$	$96.43^{+2.39}_{-0.00}$	385.1/397
Swift-XRT	00030090003	$0.248^{+0.022}_{-0.019}$	$0.221^{+0.022}_{-0.021}$	$110.15^{+97.31}_{-46.96}$	$56.4^{+8.0}_{-18.5}$	$1.90^{+0.06}_{-0.06}$	$166.86^{+14.16}_{-10.99}$	541.1/542
Swift-XRT	00030090006	$0.229^{+0.015}_{-0.013}$	$0.254^{+0.018}_{-0.018}$	$61.17^{+31.68}_{-18.72}$	$55.2^{+4.3}_{-7.9}$	$1.76^{+0.05}_{-0.05}$	$249.54^{+19.93}_{-17.23}$	729.0/643
Swift-XRT	00030090007	$0.285^{+0.013}_{-0.011}$	$0.190^{+0.009}_{-0.009}$	$272.49^{+111.52}_{-72.20}$	$76.2^{+7.5}_{-11.6}$	$1.92^{+0.03}_{-0.02}$	$166.52^{+5.71}_{-6.74}$	913.1/717
Swift-XRT	00030090009	$0.256^{+0.017}_{-0.015}$	$0.206^{+0.015}_{-0.015}$	$159.70^{+103.54}_{-57.52}$	$62.7^{+7.5}_{-12.4}$	$1.91^{+0.04}_{-0.04}$	$178.98^{+10.32}_{-9.91}$	702.8/653
Swift-XRT	00030090010	$0.250^{+0.026}_{-0.022}$	$0.220^{+0.026}_{-0.024}$	$111.33^{+125.42}_{-54.19}$	$56.1^{+6.1}_{-20.5}$	$1.88^{+0.06}_{-0.06}$	$185.64^{+15.59}_{-15.42}$	590.3/540
Swift-XRT	00030090012	$0.227^{+0.017}_{-0.015}$	$0.232^{+0.019}_{-0.019}$	$78.28^{+52.24}_{-28.34}$	$49.2^{+4.8}_{-12.4}$	$1.78^{+0.05}_{-0.05}$	$220.27^{+19.37}_{-22.31}$	743.2/642
Swift-XRT	00030090013	$0.215^{+0.020}_{-0.017}$	$0.246^{+0.028}_{-0.026}$	$47.88^{+43.45}_{-20.49}$	$38.1^{+4.2}_{-8.4}$	$1.78^{+0.06}_{-0.06}$	$201.90^{+22.41}_{-21.20}$	569.8/554
Swift-XRT	00030090015	$0.218^{+0.017}_{-0.015}$	$0.244^{+0.022}_{-0.022}$	$46.77^{+33.47}_{-17.51}$	$36.0^{+2.2}_{-11.0}$	$1.72^{+0.05}_{-0.05}$	$216.40^{+22.16}_{-18.68}$	738.9/644
Swift-XRT	00030090016	$0.250^{+0.023}_{-0.019}$	$0.225^{+0.023}_{-0.022}$	$72.45^{+65.66}_{-31.49}$	$40.3^{+4.0}_{-14.7}$	$1.81^{+0.06}_{-0.06}$	$158.85^{+13.94}_{-14.84}$	527.2/557
Swift-XRT	00030090019	$0.171^{+0.008}_{-0.008}$	–	–	–	$1.90^{+0.03}_{-0.03}$	$101.99^{+0.00}_{-1.71}$	524.9/456
Swift-XRT	00030090020	$0.154^{+0.011}_{-0.011}$	–	–	–	$1.76^{+0.04}_{-0.04}$	$84.84^{+8.83}_{-8.28}$	371.6/334
Swift-XRT	00030090021	$0.177^{+0.008}_{-0.008}$	–	–	–	$1.73^{+0.03}_{-0.03}$	$48.54^{+3.03}_{-3.27}$	536.3/481
Swift-XRT	00030090022	$0.177^{+0.008}_{-0.008}$	–	–	–	$1.69^{+0.03}_{-0.03}$	$42.70^{+3.09}_{-2.41}$	565.7/525
Swift-XRT	00030090023	$0.186^{+0.006}_{-0.006}$	–	–	–	$1.68^{+0.02}_{-0.02}$	$47.19^{+2.20}_{-2.81}$	609.8/600
Swift-XRT	00030090024	$0.174^{+0.007}_{-0.006}$	–	–	–	$1.66^{+0.02}_{-0.02}$	$39.87^{+1.91}_{-2.05}$	595.1/592
Swift-XRT	00030090026	$0.208^{+0.009}_{-0.009}$	–	–	–	$1.67^{+0.03}_{-0.03}$	$27.53^{+2.69}_{-1.52}$	554.7/522
Swift-XRT	00030090027	$0.213^{+0.020}_{-0.019}$	–	–	–	$1.65^{+0.06}_{-0.06}$	$29.12^{+3.62}_{-3.82}$	227.6/254
Swift-XRT	00030090028	$0.195^{+0.004}_{-0.004}$	–	–	–	$1.62^{+0.01}_{-0.01}$	$30.62^{+0.73}_{-0.79}$	902.7/759
Swift-XRT	00030090030	$0.208^{+0.009}_{-0.009}$	–	–	–	$1.68^{+0.02}_{-0.02}$	$25.46^{+1.89}_{-1.52}$	565.7/558
Swift-XRT	00030090031	$0.190^{+0.010}_{-0.010}$	–	–	–	$1.62^{+0.03}_{-0.03}$	$28.11^{+2.52}_{-2.18}$	536.7/466
Swift-XRT	00030090032	$0.206^{+0.017}_{-0.016}$	–	–	–	$1.66^{+0.05}_{-0.05}$	$21.02^{+2.85}_{-2.36}$	306.6/306
Swift-XRT	00030090033	$0.216^{+0.016}_{-0.015}$	–	–	–	$1.65^{+0.04}_{-0.04}$	$23.01^{+2.51}_{-2.16}$	286.4/326
Swift-XRT	00030090034	$0.177^{+0.019}_{-0.018}$	–	–	–	$1.58^{+0.05}_{-0.05}$	$29.76^{+4.81}_{-3.89}$	272.2/284

Table B. Continuing table A.

Telescope	ObsId/Ref	$N_{\rm H}$	$kT_{\rm in}$	$K_{\rm disc}$	$F_{\rm disc}$	Γ	$F_{\rm PL}$	χ^2/ν
			SWIFT J1753.5-0127 (*continuing*)					
Swift-XRT	00030090037	$0.177^{+0.007}_{-0.007}$	–	–	–	$1.65^{+0.02}_{-0.02}$	$28.47^{+1.43}_{-1.32}$	610.5/582
Swift-XRT	00030090038	$0.193^{+0.010}_{-0.009}$	–	–	–	$1.56^{+0.03}_{-0.03}$	$35.68^{+2.54}_{-2.47}$	509.6/514
Swift-XRT	00030090039	$0.181^{+0.010}_{-0.009}$	–	–	–	$1.56^{+0.03}_{-0.03}$	$34.54^{+2.17}_{-3.23}$	511.7/514
Swift-XRT	00030090040	$0.260^{+0.236}_{-0.181}$	–	–	–	$1.61^{+0.40}_{-0.36}$	$31.29^{+52.70}_{-16.34}$	12.0/9
Swift-XRT	00030090041	$0.186^{+0.009}_{-0.009}$	–	–	–	$1.61^{+0.03}_{-0.03}$	$33.98^{+1.74}_{-2.36}$	538.7/513
Swift-XRT	00030090042	$0.154^{+0.009}_{-0.009}$	–	–	–	$1.60^{+0.03}_{-0.03}$	$40.51^{+3.16}_{-3.05}$	522.9/495
Swift-XRT	00030090043	$0.173^{+0.009}_{-0.008}$	–	–	–	$1.64^{+0.03}_{-0.03}$	$31.49^{+2.38}_{-2.08}$	593.8/512
Swift-XRT	00030090044	$0.176^{+0.008}_{-0.008}$	–	–	–	$1.62^{+0.02}_{-0.02}$	$33.66^{+2.15}_{-1.83}$	650.7/553
Swift-XRT	00030090045	$0.181^{+0.008}_{-0.008}$	–	–	–	$1.63^{+0.03}_{-0.03}$	$35.23^{+2.52}_{-2.35}$	573.5/526
Swift-XRT	00030090050	$0.163^{+0.009}_{-0.009}$	–	–	–	$1.62^{+0.03}_{-0.03}$	$37.51^{+2.77}_{-2.30}$	486.3/486
			GRO J1655-40					
Swift-XRT	00030009002	$0.574^{+0.017}_{-0.017}$	–	–	–	$1.62^{+0.03}_{-0.02}$	$45.54^{+2.52}_{-3.60}$	711.8/650
Swift-XRT	00030009005	$0.662^{+0.006}_{-0.006}$	$1.482^{+0.008}_{-0.008}$	$0.64^{+0.01}_{-0.01}$	$670.7^{+2.8}_{-3.4}$	–	–	420.6/686
Swift-XRT	00030009006	$0.658^{+0.006}_{-0.006}$	$1.486^{+0.008}_{-0.008}$	$0.62^{+0.01}_{-0.01}$	$655.6^{+2.7}_{-2.8}$	–	–	432.1/686
Swift-XRT	00030009008	$0.767^{+0.030}_{-0.028}$	$1.510^{+0.030}_{-0.032}$	$0.25^{+0.02}_{-0.01}$	$284.0^{+9.1}_{-10.7}$	$2.62^{+0.17}_{-0.14}$	$111.42^{+12.63}_{-9.66}$	540.1/868
Swift-XRT	00030009009	$0.805^{+0.024}_{-0.024}$	$1.392^{+0.031}_{-0.031}$	$0.36^{+0.03}_{-0.03}$	$288.7^{+8.8}_{-8.4}$	$2.48^{+0.10}_{-0.09}$	$164.22^{+22.87}_{-17.35}$	617.2/857
Swift-XRT	00030009010	$0.787^{+0.025}_{-0.024}$	$1.439^{+0.032}_{-0.032}$	$0.31^{+0.03}_{-0.02}$	$291.5^{+7.9}_{-9.3}$	$2.51^{+0.11}_{-0.10}$	$150.93^{+24.62}_{-17.79}$	586.0/858
Swift-XRT	00030009011	$0.741^{+0.025}_{-0.026}$	$1.365^{+0.030}_{-0.029}$	$0.46^{+0.04}_{-0.04}$	$343.0^{+8.8}_{-8.5}$	$2.37^{+0.11}_{-0.10}$	$182.59^{+26.91}_{-18.07}$	567.0/856
Swift-XRT	00030009012	$0.761^{+0.048}_{-0.044}$	$1.401^{+0.055}_{-0.056}$	$0.50^{+0.08}_{-0.06}$	$415.5^{+22.4}_{-21.2}$	$2.36^{+0.27}_{-0.21}$	$202.51^{+74.82}_{-49.98}$	545.1/692
Swift-XRT	00030009014	$0.593^{+0.006}_{-0.006}$	$1.461^{+0.008}_{-0.008}$	$0.59^{+0.01}_{-0.01}$	$585.6^{+2.9}_{-2.3}$	–	–	460.2/686
Swift-XRT	00030009015	$0.749^{+0.028}_{-0.026}$	$1.364^{+0.044}_{-0.035}$	$0.80^{+0.12}_{-0.11}$	$597.3^{+87300}_{-597.3}$	–	–	456.1/684
Swift-XRT	00030009016	$0.691^{+0.032}_{-0.032}$	$1.444^{+0.065}_{-0.058}$	$0.55^{+0.11}_{-0.08}$	$521.3^{+14.7}_{-27.3}$	$1.84^{+0.20}_{-0.21}$	$584.80^{+261.76}_{-232.97}$	289.1/684
Swift-XRT	00030009018	$0.670^{+0.027}_{-0.025}$	$1.326^{+0.040}_{-0.031}$	$0.92^{+0.14}_{-0.13}$	$612.5^{+36.6}_{-47.5}$	$1.50^{+0.19}_{-0.29}$	$1424.60^{+469.92}_{-380.62}$	270.9/684
Swift-XRT	00030009019	$0.721^{+0.034}_{-0.032}$	$1.461^{+0.047}_{-0.047}$	$0.55^{+0.08}_{-0.06}$	$543.8^{+147.5}_{-140.5}$	$2.06^{+0.23}_{-0.22}$	$299.57^{+128.81}_{-68.93}$	264.7/684
Swift-XRT	00030009020	$0.621^{+0.006}_{-0.006}$	$1.520^{+0.010}_{-0.010}$	$0.65^{+0.02}_{-0.02}$	$752.7^{+3.2}_{-4.0}$	–	–	410.9/686
Swift-XRT	00030009021	$0.712^{+0.014}_{-0.014}$	$1.452^{+0.016}_{-0.016}$	$0.78^{+0.04}_{-0.03}$	$746.1^{+5.2}_{-6.4}$	–	–	885.2/696
Swift-XRT	00030009022	$0.660^{+0.013}_{-0.012}$	$1.400^{+0.015}_{-0.015}$	$0.85^{+0.04}_{-0.04}$	$701.8^{+5.3}_{-6.0}$	–	–	815.3/690
Swift-XRT	00030009023	$0.677^{+0.015}_{-0.015}$	$1.437^{+0.018}_{-0.017}$	$0.70^{+0.04}_{-0.03}$	$643.2^{+6.9}_{-7.3}$	–	–	732.8/674
Swift-XRT	00030009025	$0.681^{+0.014}_{-0.013}$	$1.191^{+0.012}_{-0.012}$	$0.99^{+0.05}_{-0.04}$	$431.0^{+3.6}_{-3.8}$	–	–	737.8/636
Swift-XRT	00030009026	$0.716^{+0.037}_{-0.021}$	$1.023^{+0.041}_{-0.024}$	$1.28^{+0.10}_{-0.16}$	$301.8^{+27.2}_{-25.3}$	$0.90^{+0.96}_{-2.55}$	$1293.49^{+0.00}_{-1293.49}$	641.9/556
Swift-XRT	00030009027	$1.504^{+0.536}_{-0.441}$	–	–	–	$0.49^{+0.23}_{-0.22}$	$593.68^{+316.52}_{-593.68}$	53.9/47
Swift-XRT	00030009028	$1.098^{+0.688}_{-0.442}$	$0.371^{+0.232}_{-0.122}$	$0.70^{+9.67}_{-0.65}$	$2.9^{+0.0}_{-2.9}$	$0.74^{+0.33}_{-0.36}$	$237.46^{+0.00}_{-128.71}$	52.1/46
Swift-XRT	00030009029	$0.636^{+0.105}_{-0.095}$	–	–	–	$1.29^{+0.13}_{-0.12}$	$30.67^{+17.35}_{-11.72}$	109.7/100
Swift-XRT	00030009031	$0.639^{+0.740}_{-0.635}$	–	–	–	$0.98^{+0.54}_{-0.48}$	$2.71^{+0.00}_{-2.71}$	10.9/9
			GX 339-4					
Swift-XRT	00030919001	$0.476^{+0.075}_{-0.056}$	$0.583^{+0.017}_{-0.016}$	$3.08^{+0.45}_{-0.53}$	$76.9^{+7.5}_{-15.2}$	$2.51^{+0.43}_{-0.81}$	$20.66^{+0.00}_{-20.66}$	332.8/332
Swift-XRT	00030919001	$0.447^{+0.084}_{-0.042}$	$0.591^{+0.020}_{-0.016}$	$3.16^{+0.37}_{-0.52}$	$83.5^{+12.8}_{-16.4}$	$2.29^{+0.56}_{-0.84}$	$23.85^{+0.00}_{-23.85}$	299.6/356
Swift-XRT	00030919002	$0.406^{+0.034}_{-0.017}$	$0.594^{+0.018}_{-0.022}$	$3.44^{+0.53}_{-0.44}$	$92.6^{+2.6}_{-4.2}$	$(0.71^{+1.75}_{-1.86})$	$(169.44^{+0.00}_{-169.44})$	301.6/278
Swift-XRT	00030919002	$0.437^{+0.082}_{-0.027}$	$0.601^{+0.018}_{-0.017}$	$3.10^{+0.38}_{-0.33}$	$87.7^{+9.9}_{-12.8}$	$2.26^{+0.82}_{-1.70}$	$8.67^{+0.40}_{-8.67}$	305.8/285
Swift-XRT	00030919003	$0.457^{+0.047}_{-0.029}$	$0.596^{+0.011}_{-0.011}$	$2.10^{+0.16}_{-0.17}$	$57.2^{+5.6}_{-4.4}$	$2.33^{+0.36}_{-0.42}$	$14.23^{+0.00}_{-3.47}$	439.5/425
Swift-XRT	00030919003	$0.461^{+0.033}_{-0.025}$	$0.591^{+0.009}_{-0.009}$	$2.18^{+0.14}_{-0.15}$	$57.5^{+4.1}_{-4.1}$	$2.33^{+0.24}_{-0.27}$	$17.70^{+0.89}_{-2.26}$	561.4/480
Swift-XRT	00030919004	$0.504^{+0.046}_{-0.043}$	$0.595^{+0.010}_{-0.009}$	$1.66^{+0.19}_{-0.24}$	$45.0^{+4.1}_{-3.9}$	$2.66^{+0.21}_{-0.27}$	$17.46^{+0.86}_{-2.28}$	600.5/494
Swift-XRT	00030919005	$0.434^{+0.156}_{-0.044}$	$0.559^{+0.017}_{-0.017}$	$4.62^{+0.57}_{-1.71}$	$97.7^{+0.9}_{-87.6}$	$2.50^{+0.78}_{-0.52}$	$24.39^{+5.49}_{-24.39}$	361.4/323
Swift-XRT	00030919006	$0.421^{+0.072}_{-0.035}$	$0.547^{+0.024}_{-0.023}$	$2.77^{+0.43}_{-0.38}$	$53.7^{+6.0}_{-8.7}$	$2.12^{+0.59}_{-0.76}$	$19.69^{+6.23}_{-19.69}$	317.6/293
Swift-XRT	00030919006	$0.461^{+0.083}_{-0.057}$	$0.543^{+0.010}_{-0.018}$	$2.69^{+0.43}_{-0.60}$	$50.4^{+8.4}_{-9.5}$	$2.57^{+0.43}_{-0.56}$	$16.98^{+1.78}_{-5.13}$	352.3/324
Swift-XRT	00030919007	$0.411^{+0.038}_{-0.032}$	$0.441^{+0.032}_{-0.034}$	$2.79^{+0.98}_{-0.65}$	$22.9^{+3.0}_{-3.0}$	$1.90^{+0.28}_{-0.31}$	$31.38^{+8.79}_{-11.96}$	281.8/291
Swift-XRT	00030919007	$0.457^{+0.042}_{-0.039}$	$0.379^{+0.037}_{-0.043}$	$5.35^{+3.03}_{-1.60}$	$24.0^{+4.0}_{-4.7}$	$2.36^{+0.21}_{-0.23}$	$27.34^{+2.30}_{-2.99}$	314.1/305
Swift-XRT	00030919008	$0.427^{+0.024}_{-0.022}$	$0.351^{+0.024}_{-0.025}$	$3.92^{+1.58}_{-1.02}$	$12.9^{+1.3}_{-1.4}$	$2.03^{+0.12}_{-0.12}$	$21.45^{+2.95}_{-3.27}$	402.7/415
Swift-XRT	00030919008	$0.441^{+0.022}_{-0.021}$	$0.331^{+0.023}_{-0.024}$	$5.44^{+2.31}_{-1.41}$	$14.0^{+1.0}_{-1.3}$	$2.16^{+0.10}_{-0.10}$	$20.43^{+1.79}_{-1.28}$	574.9/496
Swift-XRT	00030919009	$0.406^{+0.021}_{-0.021}$	–	–	–	$2.36^{+0.06}_{-0.06}$	$22.99^{+1.77}_{-1.42}$	256.3/241
Swift-XRT	00030919010	$0.353^{+0.029}_{-0.026}$	$0.343^{+0.049}_{-0.046}$	$1.86^{+1.93}_{-0.84}$	$5.6^{+0.7}_{-1.8}$	$1.70^{+0.08}_{-0.09}$	$49.65^{+8.54}_{-5.85}$	487.6/464
Swift-XRT	00030919011	$0.344^{+0.051}_{-0.049}$	$0.626^{+0.144}_{-0.100}$	$0.08^{+0.08}_{-0.04}$	$2.5^{+0.2}_{-0.8}$	$(0.07^{+0.33}_{-0.48})$	$(1811.88^{+0.00}_{-1811.88})$	158.7/165
Swift-XRT	00030919011	$0.431^{+0.074}_{-0.062}$	$0.459^{+0.093}_{-0.079}$	$0.22^{+0.33}_{-0.12}$	$2.1^{+0.3}_{-0.8}$	$(0.66^{+0.24}_{-0.28})$	$(236.73^{+268.48}_{-236.73})$	168.6/162

Table C. Continuing table B.

Telescope	ObsId/Ref	$N_{\rm H}$	$kT_{\rm in}$	$K_{\rm disc}$	$F_{\rm disc}$	Γ	$F_{\rm PL}$	χ^2/ν
				GX 339-4 (*continuing*)				
Swift-XRT	00030919012	$0.353^{+0.024}_{-0.023}$	–	–	–	$1.84^{+0.06}_{-0.06}$	$16.23^{+2.75}_{-1.91}$	242.8/233
Swift-XRT	00030919013	$0.305^{+0.042}_{-0.038}$	–	–	–	$1.65^{+0.09}_{-0.09}$	$15.26^{+3.95}_{-3.48}$	91.2/100
Swift-XRT	00030919013	$0.209^{+0.148}_{-0.135}$	–	–	–	$1.46^{+0.34}_{-0.31}$	$23.79^{+41.85}_{-11.42}$	23.9/16
Swift-XRT	00030919013	$0.307^{+0.050}_{-0.046}$	–	–	–	$1.64^{+0.12}_{-0.11}$	$15.09^{+4.16}_{-3.49}$	69.3/77
Swift-XRT	00030943002	$0.229^{+0.028}_{-0.026}$	–	–	–	$1.37^{+0.06}_{-0.06}$	$14.31^{+3.24}_{-2.32}$	192.8/189
Swift-XRT	00030943002	$0.273^{+0.030}_{-0.028}$	–	–	–	$1.42^{+0.07}_{-0.06}$	$12.32^{+4.06}_{-1.77}$	160.8/184
Swift-XRT	00030953003	$0.255^{+0.039}_{-0.035}$	–	–	–	$1.34^{+0.08}_{-0.08}$	$16.09^{+4.30}_{-3.27}$	116.7/132
Swift-XRT	00030953007	$0.305^{+0.043}_{-0.039}$	–	–	–	$1.39^{+0.08}_{-0.08}$	$34.66^{+9.43}_{-5.74}$	99.5/132
Swift-XRT	00030953012	$0.295^{+0.031}_{-0.029}$	–	–	–	$1.48^{+0.06}_{-0.06}$	$35.93^{+5.49}_{-5.35}$	185.9/184
Swift+XTE	Spec. 1 (T08)	$0.850^{+0.070}_{-0.070}$	$0.178^{+0.007}_{-0.007}$	76^{+39}_{-26}	27.3	$1.69^{+0.01}_{-0.01}$	27.00	532.0/211
Swift+XTE	Spec. 2 (T08)	$0.900^{+0.110}_{-0.110}$	$0.157^{+0.011}_{-0.011}$	35^{+30}_{-18}	4.6	$1.64^{+0.02}_{-0.02}$	9.20	280.1/211
ASCA G+S	42010010	*0.43*	$0.214^{+0.060}_{-0.049}$	$1.13^{+4.99}_{-0.84}$	$0.51^{+0.12}_{-0.51}$	$1.63^{+0.02}_{-0.03}$	$10.03^{+0.03}_{-0.06}$	1030.70/954
ASCA G+S	42010000	*0.43*	$0.171^{+0.042}_{-0.033}$	$7.76^{+31.84}_{-5.88}$	$1.44^{+0.00}_{-1.44}$	$1.63^{+0.01}_{-0.02}$	$17.51^{+0.61}_{-0.47}$	1201.70/1174
ASCA G+S	43001000	*0.43*	$0.279^{+0.009}_{-0.009}$	$2.68^{+0.48}_{-0.38}$	$3.43^{+0.20}_{-0.02}$	$1.67^{+0.01}_{-0.01}$	$46.33^{+0.84}_{-0.87}$	2506.09/1469
XMM+XTE	M06	$0.37^{+0.05}_{-0.05}$	$0.38^{+0.01}_{-0.01}$	$0.64^{+0.08}_{-0.08}$	2.9	$1.46^{+0.01}_{-0.01}$	156.26	3899.2/2256
				XTE J1118+480				
SAX L+M+P	21173001	$0.013^{+0.002}_{-0.002}$	$0.062^{+0.012}_{-0.009}$	$780.65^{+1653.72}_{-33.54}$	$2.42^{+1.36}_{-0.77}$	$1.748^{+0.007}_{-0.007}$	$37.13^{+0.52}_{-0.69}$	213.65/189
SAX L+M+P	211730012	$0.011^{+0.001}_{-0.001}$	$0.066^{+0.007}_{-0.006}$	$992.35^{+931.64}_{-471.18}$	$2.96^{+0.40}_{-0.86}$	$1.762^{+0.006}_{-0.007}$	$28.73^{+0.37}_{-0.58}$	237.99/189
EUVE+XTE	(MC01)	*0.013*	$0.024^{+0.002}_{-0.004}$	7.e5	51.91	$1.782^{+0.005}_{-0.005}$	41.7	–
Idem+CXC+SAX	(Ch03)	$0.011^{+0.002}_{-0.002}$	$0.024^{+0.002}_{-0.03}$	$6.6^{+2.2}_{-0.9}$e5	44.85	$1.8^{+0.1}_{-0.1}$	40.	–
CXC+HST	(MC03a)	*0.012*	$1.1^{+0.2}_{-0.2}$e−3	5.4e6	1.72e−3	$2.02^{+0.16}_{-0.16}$	1.8e−4	–
				A0620-00				
CXC+HST	(MC03a)	*0.019*	7.7e−4	2.8e8	2.3e−2	$2.26^{+0.18}_{-0.18}$	4.3e−4	–